ACS OMEGA

Open Access



http://pubs.acs.org/journal/acsodf

Article

# $MoS_2$, $WS_2$, and $MoWS_2$ Flakes as Reversible Host Materials for Sodium-Ion and Potassium-Ion Batteries

Arijit Roy,* Sonjoy Dey, and Gurpreet Singh*

Cite This: *ACS Omega* 2024, 9, 24933−24947

Read Online

ACCESS | Metrics & More | Article Recommendations | Supporting Information

**ABSTRACT:** Transition-metal dichalcogenides (TMDs) and their alloys are vital for the development of sustainable and economical energy storage alternatives due to their large interlayer spacing and hosting ability for alkali-metal ions. Although the Li-ion chemically correlates with the Na-ion and K-ion, research on batteries with TMD anodes for $K^+$ is still in its infancy. This research explores TMDs such as molybdenum disulfide ($MoS_2$) and tungsten disulfide ($WS_2$) and TMD alloys such as molybdenum tungsten disulfide ($MoWS_2$) for both sodium-ion batteries (NIBs) and potassium-ion batteries (KIBs). The cyclic stability test analysis indicates that in the initial cycle, the $MoS_2$ NIB demonstrates exceptional performance, with a peak charge capacity of 1056 mAh $g^{-1}$, while retaining high Coulombic efficiency. However, the $WS_2$ KIB underperforms, with the least charge capacity of 130 mAh $g^{-1}$ in the first cycle and exceptionally low retention at a current density of 100 mA $g^{-1}$. The $MoWS_2$ TMD alloy exhibits a moderate charge capacity and cyclic efficiency for both NIBs and KIBs. This comparison study shows that decreasing sizes of alkali-metal ions and constituent elements in TMDs or TMD alloys leads to decreased resistance and slower degradation processes as indicated by cyclic voltammetry and electrochemical impedance spectroscopy after 10 cycles. Furthermore, the study of probable electrochemical intercalation and removal processes of Na-ions and K-ions demonstrates that large geometrically shaped TMD flakes are more responsive to intercalation for Na-ions than K-ions. These performance comparisons of different TMD materials for NIBs and KIBs may promote the future development of these batteries.

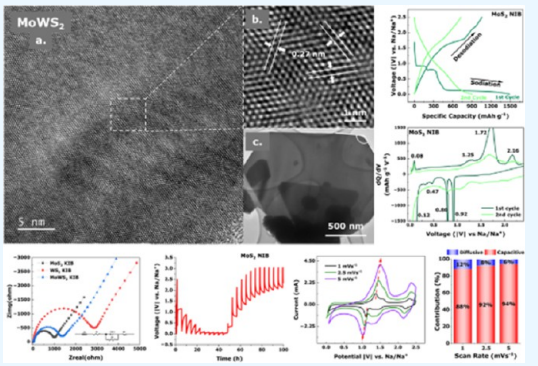


## INTRODUCTION

The invention and subsequent commercial success of lithium-ion batteries (LIBs) have powered modern consumer electronics and the transportation industry due to the use of low-cost graphite as an anode material for LIBs; graphite can cycle Li-ions for hundreds of cycles with nearly 100% efficiency.[1] However, the pursuit of sustainable electrochemical energy storage systems for renewable energy integration, as well as increasing global supply chain constraints regarding LIB constituents (e.g., lithium, cobalt, and nickel), requires batteries that are built using renewable sources and environmentally friendly materials.[2] Consequently, increased research has focused on other alkali-metal-ion-based batteries, such as sodium-ion batteries (NIBs) and potassium-ion batteries (KIBs), because sodium and potassium have more uniform, abundant distribution in the Earth crust compared to a mere 0.0017 wt %[3,4] of lithium. Recent studies have suggested several potential cathode materials and low-cost electrolyte salts for NIBs and KIBs that are analogous to those in use for commercial LIBs.[5−7] However, a suitable anode has yet to be found because Na/graphite and K/graphite compounds may not be thermodynamically stable.[8−11] Other studies have concluded that the larger radius of the Na-ion (1.02 Å) and K-ion (1.38 Å) compared to that of the Li-ion (0.76 Å) could be the reason for low capacity and poor cycling stability for NIBs and KIBs when graphite is used as the anode.[10−13] Although recent findings involving other forms of carbon, such as carbon black,[14] microcrystalline structured carbon,[15] and cellulose-derived carbon[16] as electrodes or protective layers for electrodes and those involving the use of emerging polymer[17,18] or ionic liquid electrolytes,[19−22] have yielded promising results in NIBs and KIBs,[23−25] the search for a commercially viable electrode architecture is far from over.

This search for an ideal anode for NIBs and KIBs has led to increased interest in other layered lamellar structures, including transition-metal dichalcogenides (TMDs) that have similar morphology to graphite but increased interlayer spacings.[26] Approximately 40 different TMDs have been discovered so far, of which group VI is predominantly layered; examples include molybdenum ($MoS_2$) and tungsten dichalcogenides ($WS_2$).[27−29] $MoS_2$ has been investigated extensively for LIBs and NIBs[30] along with the development of modified

Received: February 28, 2024
Revised: May 15, 2024
Accepted: May 20, 2024
Published: May 30, 2024

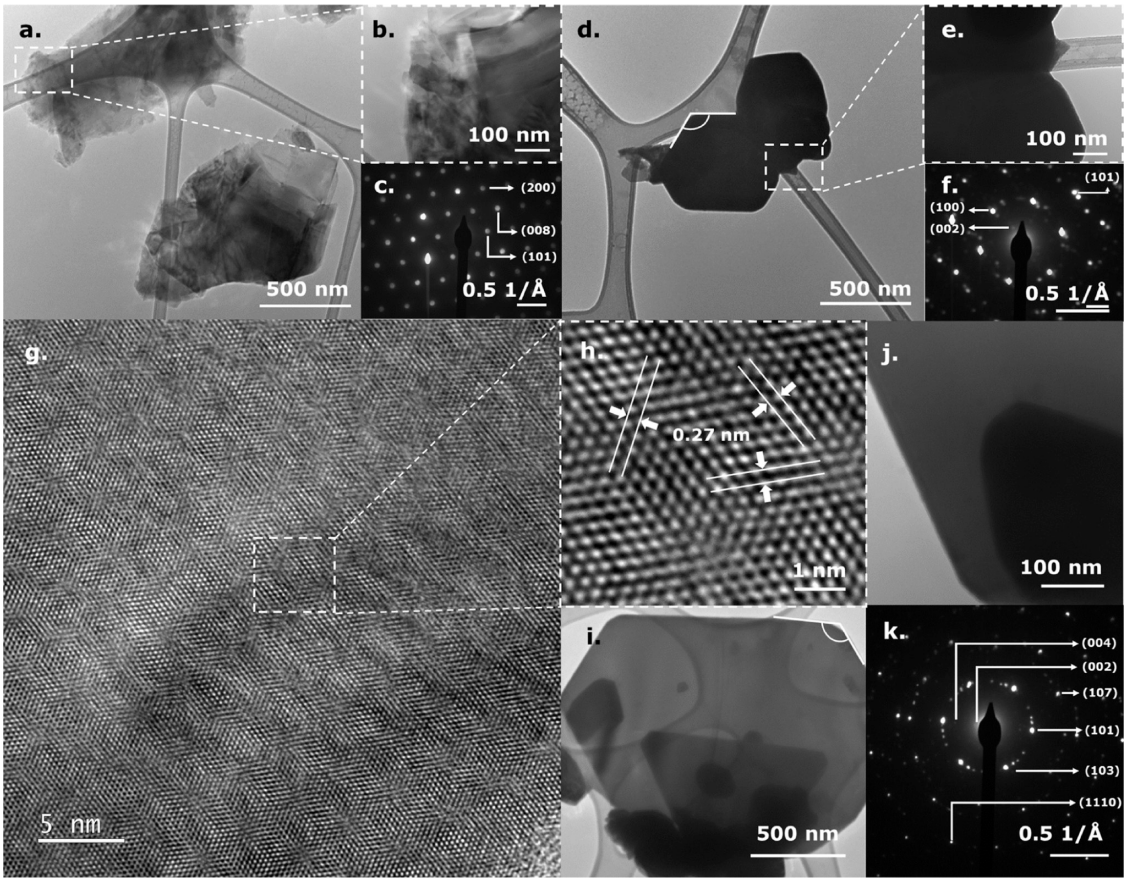


**Figure 1.** Low-resolution TEM images of (a, b) $MoS_2$ nanosheets and (c) corresponding SAED pattern; low-resolution TEM images of (d, e) $WS_2$ powders and (f) corresponding SAED pattern; high-resolution TEM images of (g, h) $MoWS_2$ powders depicting fringe distances; low-resolution TEM images of (i, j) $MoWS_2$ powders and (k) corresponding SAED pattern.

nanostructures such as nanotubes,[31] nanosheets,[32] nanoflowers,[33] nanoboxes,[34] nanospheres,[35] etc. Also, the few studies that have utilized $WS_2$ for NIBs used various modified micro/nanostructures of $WS_2$,[36,37] including hollow microspheres,[38] nanoplates,[39] and $WS_2$-3DrGO.[40] However, by alloying and doping different transition metals or chalcogen atoms, TMD alloys (i.e., $Mo_{1-x}W_xS_2$) have been shown to bring flexibility to the crystal structure and physical properties, which may unveil tunable band gaps as a function of layers.[41] For example, the tuning range of the band gap is 1.8−2.0 eV for $MoWS_2$[42] compared to $MoS_2$ with a band gap of 1.9 eV[43] and $WS_2$ with a band gap of 2.1 eV.[44] Tunability of such a band gap allows better charge transfer and higher conductivity, leading to improved specific capacitance and energy density.[45] In another recent study, an enlarged interlayer spacing of $Mo_{1-x}W_xS_2$ nanosheets indicated superior hydrogen evolution reaction (HER) performance,[46] which suggests that doping TMDs with other transition-metal ions improves the efficacy of TMD alloys as catalysts.[47] The range of band gaps and improved HER performance indicate superior prospects for TMDs and TMD alloys in future energy storage development.

Although TMDs and TMD alloys have shown promising electrode material properties, structural aggregation, electrochemical instability, low reversibility, and rapid capacity decline have always been a challenge.[26] This work investigated and compared the electrochemical performance of $WS_2$, $MoS_2$, and $MoWS_2$ nanosheets as working electrodes in half-cells of KIBs and NIBs. The interpretation of internal structural distortion and performance consistency has also been focused on in this work to compare the commonly studied TMDs ($WS_2$ and $MoS_2$) with the rarely investigated $MoWS_2$ TMD alloy as an electrode for NIBs and KIBs. This study employed cyclic voltammetry (CV) and electrochemical impedance spectroscopy (EIS) to comprehend faradaic and non-faradaic contributions, the effect of scan rate, and cell degradation processes. A comparison with a previous study on $MoWSe_2$ electrodes[48] revealed significant insight into the role of the atomic size of the constituent elements in the TMDs and TMD alloys.

Analysis of the cyclic stability test revealed that the $MoS_2$ NIB has the highest charge capacity of 1056 mAh $g^{-1}$ in the first cycle, with the highest retention capacity of 71%, while the $WS_2$ KIB has the lowest charge capacity of 130 mAh $g^{-1}$ in the first cycle and only 29% retention capacity at a current density of 100 mA $g^{-1}$. The $MoWS_2$ TMD alloy showed intermediate charge capacity and cyclic efficiency for both NIBs and KIBs.

## MATERIALS, METHODS, AND CHARACTERIZATION

**Morphologic and Spectroscopic Characterization.** In this study, all of the scanning electron microscopy (SEM) images were obtained using a Hitachi SU8010 microscope, and the X-ray fluorescence (XRF) spectrum was collected using the IXRF system on a Hitachi SEM, which is equipped with an X-ray fluorescence and detection capability. Also, transmission electron microscopy (TEM) of the bulk $MoS_2$, $WS_2$, and


https://doi.org/10.1021/acsomega.4c01966
ACS Omega 2024, 9, 24933−24947

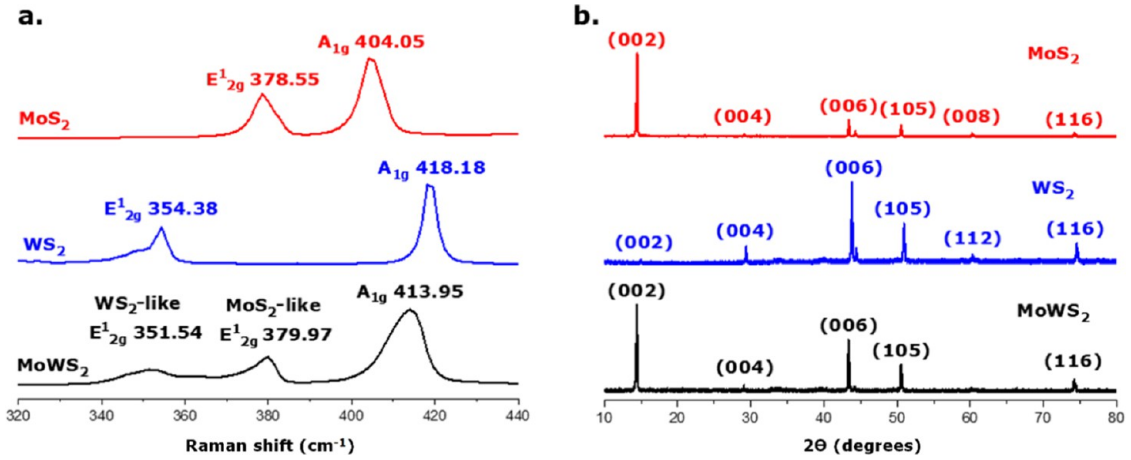


**Figure 2.** (a) Raman spectra of $MoS_2$, $WS_2$, and $MoWS_2$ powders and (b) XRD reflection of $MoS_2$, $WS_2$, and $MoWS_2$ electrodes.

$MoWS_2$ was carried out using an FEI Tecnai Osiris 200 kV, and the Philips CM100 microscope was used for selected area electron diffraction (SAED) images. A Renishaw inVia Raman microscope was used to collect Raman spectra with a 532 nm laser. The Thermo Fisher scientific instrument was used to obtain X-ray photoelectron spectroscopy (XPS) data, equipped with a monochromatic Al anode K$\alpha$ ($h\nu$ = 1486.6 eV) with in situ sputtering of $Ar^+$ at 3.0 keV for 120 s. The PANalytical Empyrean was used to collect X-ray diffraction (XRD) data at 45 kV, a 40 mA power setting, and a step size of 0.02°.

**Electrochemical Characterization.** All of the electrodes in this study ($MoS_2$, $WS_2$, and $MoWS_2$) were prepared using a similar wt % ratio. 70 wt % of $MoS_2$, $WS_2$, or $MoWS_2$ powder as received (Ossila, Sheffield, U.K.) were mixed with 15 wt % of carbon black (Alfa Aesar, MA) as conducting agent and 15 wt % of polyvinylidene fluoride (Alfa Aesar, MA) as binder. All of the mass measurements were conducted using an analytical balance with a readability of 0.1 mg and a repeatability of 0.08 mg. A few drops of *N*-methyl-2-pyrrolidinone (Sigma-Aldrich, MO) were also mixed as a solvent to obtain a homogeneous slurry, which was coated onto a Cu foil (thickness = 9 $\mu$m). After the samples were dried overnight at 80 °C, circular electrodes with a diameter of 14.29 mm were punched out from the coated Cu foils. These circular electrodes at an active mass loading of approximately 0.5 mg $cm^{-2}$ were used as working electrodes, while the counter electrodes were made of Na and K metals for Na-ion and K-ion half-cells, respectively. One M $NaClO_4$ (Alfa Aesar) in (1:1 v/v) ethylene carbonate (EC)/dimethyl carbonate (DMC) (anhydrous, 99% Sigma-Aldrich) and 1.0 M $KPF_6$ (Alfa Aesar) in (1:1 v/v) EC/DMC were used as electrolytes for NIBs and KIBs, respectively. At high precision in an inert Ar atmosphere (inside the glovebox), the coin cells (CR-2032) were assembled, where the $O_2$ and $H_2O$ contents were kept below 0.1 ppm throughout the process. The electrochemical behavior of the assembled cells was investigated using the Arbin BT 2000 test unit (four channels in current ranges: 0.1, 0.001, and 0.00001 A with a maximum channel power of 1 W). The cyclic stability test was carried out with a current density of 100 mAh $g^{-1}$. The electrochemical workstation from CH Instruments (model CHI660E) was used to carry out the cyclic voltammetry (CV) tests and electrochemical impedance spectroscopy (EIS). Based on the manufacturer's specifications, the electrochemical workstation has applied potential and current measurement accuracy of ±1 mV (±0.01% of scale) and 0.2%, respectively. The measured current resolution is 0.0015% of the current range (minimum of 0.3 fA). Then, the cycled half-cells were decrimped in a similar Ar atmosphere, and the recovered electrodes were dried at 80 °C for 24 h.

## RESULTS AND DISCUSSION

The lateral size, morphology, and crystallinity of $MoS_2$, $WS_2$, and $MoWS_2$ powders were studied by transmission electron microscopy (TEM) and high-resolution TEM (HRTEM). Figure 1a–c shows the TEM image for $MoS_2$, Figure 1d–f shows $WS_2$, and Figure 1g–k shows $MoWS_2$. The thin sheet-like morphology and rough edges of thin $MoS_2$ flakes are evident in Figure 1a,b; these were likely the result of the TEM sample preparation process (i.e., liquid exfoliated flakes suspended on a lacey carbon grid). The corresponding selected area electron diffraction (SAED) pattern of the $MoS_2$ sample (Figure 1c) revealed a six-spot hexagonal pattern with (101), (008), and (200) planes,[49] indicating the crystallinity. For the $WS_2$ nanosheets, the layered structure with a 120° edge angle was apparent, which is typical of TMD materials, as shown in Figure 1d,e. The corresponding SAED pattern in Figure 1f showed (002), (100), and (101) planes, which validate a well-crystalline structure.[29] The high-resolution TEM images taken along the edges of the $MoWS_2$ nanosheets showed densely packed stripe-like overlapping grains (Figure 1g). Figure 1h derived from Figure 1g is analyzed via fast Fourier transformation (FFT), inverse FFT based on bright spots, and fringe intensity profile to investigate the interfringe distance. These analyses revealed the crystal symmetry of the $MoWS_2$ nanosheets with a lattice constant of approximately 0.27 nm, which was in agreement with the interlayer lattice spacing value of the (100) plane from $MoS_2$ and $WS_2$. The low-resolution TEM image in Figure 1i,j demonstrates the existence of triangular domains, which is typical of layered group VI TMD materials.[50] The subsequent SAED pattern of such a domain (Figure 1k) exhibited a six-spot hexagonal pattern with a combination of $MoS_2$-like (002), (101), and (107) and $WS_2$-like (004), (103), and (1110) planes. Overall, the TMD flakes were approximately 1–2 $\mu$m in size, which matched the manufacturer's specifications.

Figure 2a shows the Raman spectra of the as-obtained $MoS_2$, $WS_2$, and $MoWS_2$ powders. The Raman spectrum of $MoS_2$ demonstrates prominent $E_{2g}^1$ and $A_{1g}$ modes at 378.55 and 404.05 $cm^{-1}$, respectively.[51] For the neat $WS_2$, the high-


https://doi.org/10.1021/acsomega.4c01966
ACS Omega 2024, 9, 24933−24947

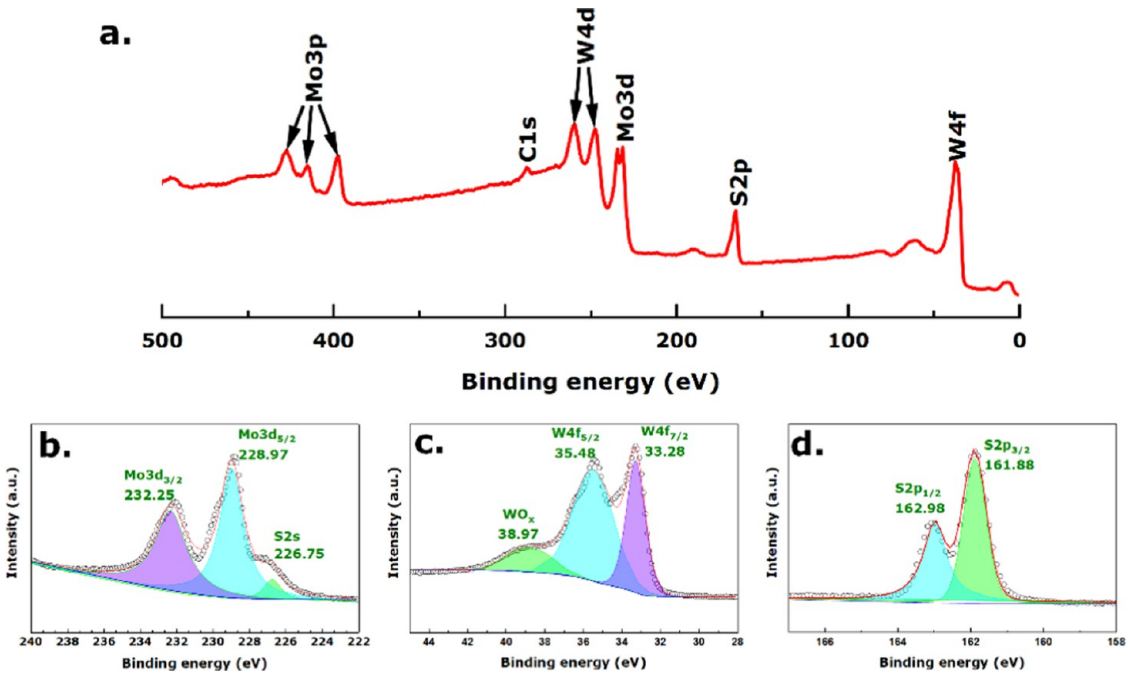


**Figure 3.** (a) XPS survey scan representing the presence of different elements within $MoWS_2$; high-resolution (b) Mo 3d, (c) W 4f, and (d) S 2p XPS spectra of the $MoWS_2$ material demonstrating the chemical bonding states.

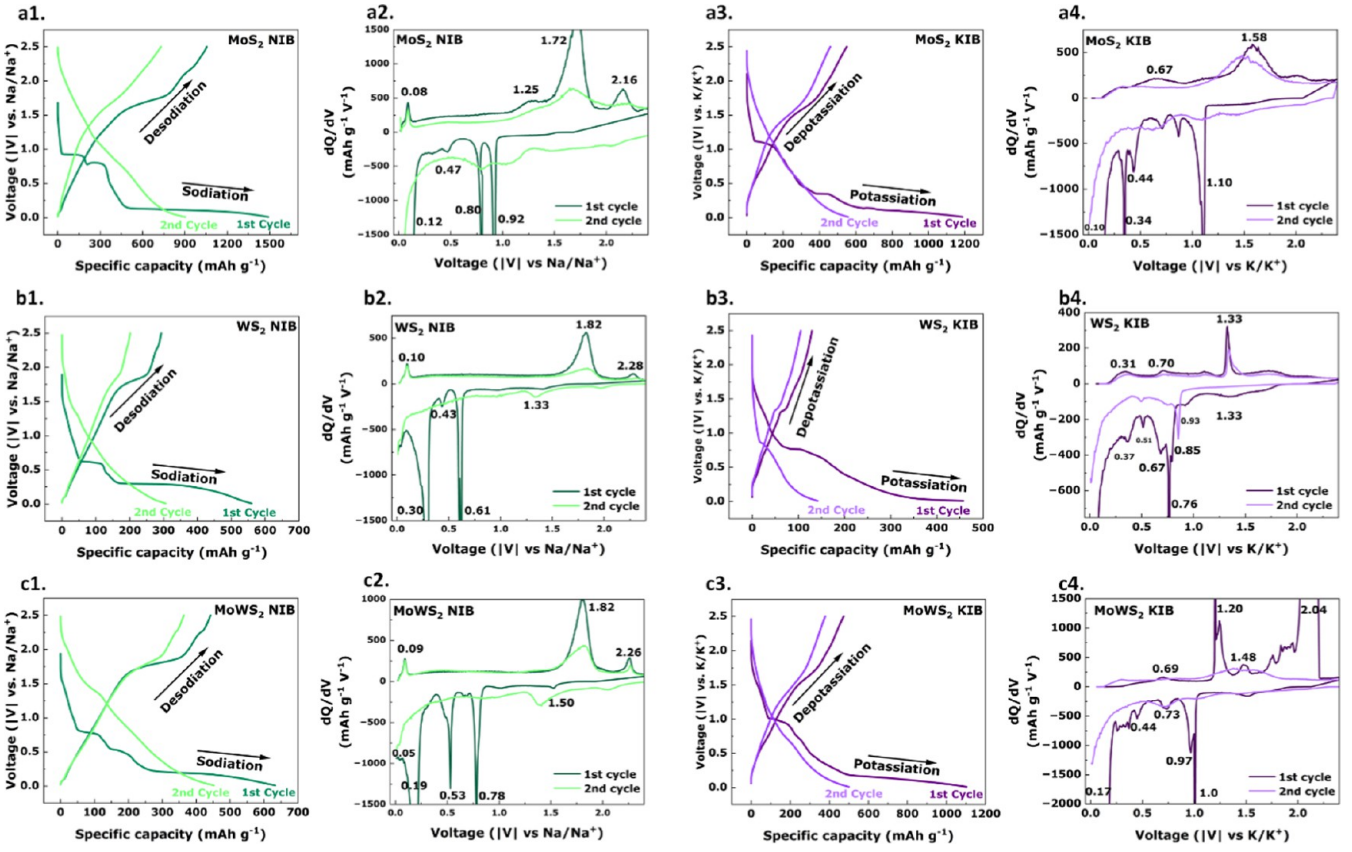


**Figure 4.** (a1) GCD and (a2) differential capacity curves of $MoS_2$ NIB electrodes; (a3) GCD and (a4) differential capacity curves of $MoS_2$ KIB electrodes; (b1) GCD and (b2) differential capacity curves of $WS_2$ NIB electrodes; (b3) GCD and (b4) differential capacity curves of $WS_2$ KIB electrodes; (c1) GCD and (c2) differential capacity curves of $MoWS_2$ NIB electrodes, and (c3) GCD and (c4) differential capacity curves of $MoWS_2$ KIB electrodes.

intensity $E_{2g}^1$ and $A_{1g}$ modes were at 354.38 and 418.18 $cm^{-1}$, respectively.[29] While the in-plane $E_{2g}^1$ vibration mode denoted the optical vibration of transition metals and chalcogen atoms, the out-of-plane $A_{1g}$ vibration denoted the optical vibration of



https://doi.org/10.1021/acsomega.4c01966
ACS Omega 2024, 9, 24933−24947

chalcogen atoms. These observations are consistent with the literature for high-purity bulk crystals. For the $MoWS_2$ alloy sample, the mode at 413.95 $cm^{-1}$ was assigned to $A_{1g}$ because it was between the $A_{1g}$ modes of $MoS_2$ and $WS_2$. The other two prominent peaks at 351.54 and 379.97 $cm^{-1}$ were assigned to $WS_2$ and $MoS_2$-like $E_{2g}{}^1$ modes, respectively.[52] This observation differs from previous works involving $Mo_xW_{1-x}S_2$ ultrathin sheets, which reported two Raman bands for bulk $MoWS_2$ instead of the three bands reported in this study. Nonetheless, shifting of the $A_{1g}$ mode of $MoS_2$ to a higher wavenumber due to W doping in the $MoS_2$ $E_{2g}{}^1$ mode was noted.[53] This two-mode behavior of $MoWS_2$ can be correlated with a 1.92 times larger atomic weight of W compared to Mo since this mass difference causes both metal atoms to vibrate.[54]

X-ray diffraction (XRD) was utilized on materials coated on Cu foils to identify the crystallinity of the $MoS_2$, $WS_2$, and $MoWS_2$ electrodes (Figure 2b). For the $MoS_2$ sample, peaks at 14.49, 29.12, 43.40, 50.54, 60.22, and 74.18° were ascribed to the (002), (004), (006), (105), (008), and (116) crystal planes,[55] respectively (JCPDS card no. 00-037-1492). However, reflections from $WS_2$ suggested peaks at 14.14, 29.35, 43.79, 50.92, 60.30, and 74.55°, indicating the existence of (002), (004), (006), (105), (112), and (116) crystal planes,[56] respectively (JCPDS card no. 00-008-0237). The $MoWS_2$ electrode demonstrated a mix of reflections from $MoS_2$ and $WS_2$; specifically, (002), (004), (006), (105), and (116) crystal planes occurred in the diffractogram with *d*-spacings of 6.14, 3.07, 2.09, 1.81, and 1.28 Å, respectively.[57]

X-ray photoelectron spectroscopy (XPS) of the electrodes showed surface characteristics with the chemical and electronic states of the material. Figure 3a shows the XPS survey scan of $MoWS_2$, while Figure 3b−d shows the high-resolution scans of the Mo 3d, W 4f, and S 2p spectra, respectively. In Figure 3b, the Mo 3d high-resolution spectral deconvolution reveals one peak of Mo $3d_{3/2}$ at 232.25 eV and another peak of Mo $3d_{5/2}$ at 228.97 eV, both attributed to $MoS_2$.[58] Additionally, at higher binding energy for oxidized $MoS_2$, the ion contributions were nearly identical, such as $MoO_2$ and $MoO_3$.[59] In the fitted high-resolution W 4f spectra (Figure 3c), two peaks at 33.28 and 35.48 eV were identified for W $4f_{7/2}$ and W $4f_{5/2}$, respectively, which were ascribed to the +4 valence state of tungsten.[60] Another peak at 38.97 eV indicated the presence of $WO_x$ due to partial oxidization.[61] The S $2p_{3/2}$ and S $2p_{1/2}$ peaks at 161.88 and 162.98 eV binding energies, respectively, defined the divalent states of metal sulfide.[62]

Galvanostatic charge−discharge (GCD) and differential or incremental capacity curves derived from GCD curves revealed reactions at various stages during charging and discharging cycles. Figure 4a1 shows GCD plots for the $MoS_2$ NIB half-cell for the first two cycles with the first-cycle differential capacity curve (Figure 4a2), showing specific peaks at 0.92, 0.8, 0.47, and 0.12 V during sodiation. Although the 0.92 and 0.8 V peaks could be ascribed to the insertion of Na-ions into $MoS_2$ layers, the 0.47 V peak could be due to the conversion reaction between Na-ions and $Na_xMoS_2$. The remaining 0.1 V peak may be the result of a solid electrolyte interphase (SEI) layer on $MoS_2$ during initial sodiation since the intensity of forming the SEI layer decreased in the consecutive sodiation cycle.[63] In the second cycle, the 0.92 V peak showed slight polarization, moving to 1.02 V, and in the first desodiation process, peaks were visible at 0.08, 1.25, 1.72, and 2.16 V, potentially due to reverse insertion and conversion reactions during desodiation.

The GCD curves (Figure 4a3) and derived differential capacity curves (Figure 4a4) highlight the potassiation/depotassiation reactions at different voltages. In the first potassiation process, the peaks at 1.10 and 0.44 V may be attributed to K-ions intercalating into $MoS_2$ layers and conversion reactions to generate Mo and $K_2S$. These peaks lost their intensity in the second cycle onward. Other peaks in the 0.01−0.3 V range could be due to irreversible SEI formation. Reversible intercalation and conversion reaction peaks were visible in the depotassiation process at 0.67 and 1.58 V, similarly losing intensity from the second cycle onward.[64]

Figure 4b1 depicts the GCD curves from which the differential capacity curves (Figure 4b2) of the $WS_2$ NIB half-cells were derived. The first-cycle sodiation curve showed peaks at 0.61, 0.43, and 0.30 V. Although the peak at 0.61 V may be attributed to the insertion of $Na^+$ into $WS_2$ to form $Na_xWS_2$, the other two peaks at 0.43 and 0.30 V could be ascribed to the conversion reaction and SEI layer formation. In the first-cycle desodiation process, peaks at 1.82 and 2.28 V could be attributed to sodium extraction and back conversion reaction, forming W to $WS_2$.[65] In the second cycle, the insertion and conversion reactions moved to 1.96 and 1.33 V during sodiation, respectively, but in the second cycle, desodiation process, $Na^+$ extraction, and reverse conversion peaks demonstrated slight polarization behavior, moving to 1.83 and 2.3 V, respectively, with much lower intensity.

First-cycle potassiation and depotassiation GCD curves (Figure 4b3) and derived differential capacity curves (Figure 4b4) depicted the $K^+$ interaction with the $WS_2$. In the first-cycle potassiation, peaks appeared at 1.33, 0.93, 0.76, 0.67, 0.51, and 0.37 V. Peaks on or above 0.76 V may be attributed to the insertion of K-ions into the $WS_2$ lattice to form $K_xWS_2$, while the peaks below 0.76 V may be ascribed to the conversion reaction to form $K_xS$ and metallic W and the construction of the SEI film. In the depotassiation process, peaks formed at 1.33, 0.70, and 0.31 V, with the broad peak at 1.33 V potentially signifying the extraction of K-ions from $WS_2$ and the other peaks signifying the reverse conversion reaction.[66] In the second-cycle potassiation process, the insertion and conversion reaction peaks moved to 0.85 and 0.50 V, respectively.[29]

For the $MoWS_2$ nanosheets, the GCD curves (Figure 4c1) and derived differential capacity curves (Figure 4c2) illustrated multistep reactions during the sodiation/desodiation process. During the first sodiation cycle, the peaks at 1.5 and 0.05 V may correlate with the alloy insertion and conversion reactions within $MoS_2$ lattices. Because the peaks at 0.78, 0.53, and 0.19 V were absent in the subsequent cycle, they were ascribed to irreversible SEI layer formation.[67] In the first desodiation process, broad peaks at 2.26 and 1.82 V were attributed to $Na^+$ extraction and reverse conversion reaction from both $WS_2$ and $MoS_2$ lattices within the $MoWS_2$ alloy, while in the second cycle, a pair of peaks appeared at 1.39/1.83 and 2.07/2.26 V during the sodiation/desodiation processes, similar to neat $MoS_2$ and $WS_2$ electrodes.

The first cycle of potassiation/depotassiation GCD (Figure 4c3) and derived differential capacity curves (Figure 4c4) contained multiple peaks that resembled both $MoS_2$ and $WS_2$ electrodes. For example, the first-cycle potassiation step exhibited $WS_2$-like reactions at 0.9−1.0 and 0.73 V and $MoS_2$-like reactions at 0.44 V. The first depotassiation step resulted in broad peaks at the 1.9−2.2 and 1.17−1.30 V


https://doi.org/10.1021/acsomega.4c01966
ACS Omega 2024, 9, 24933−24947

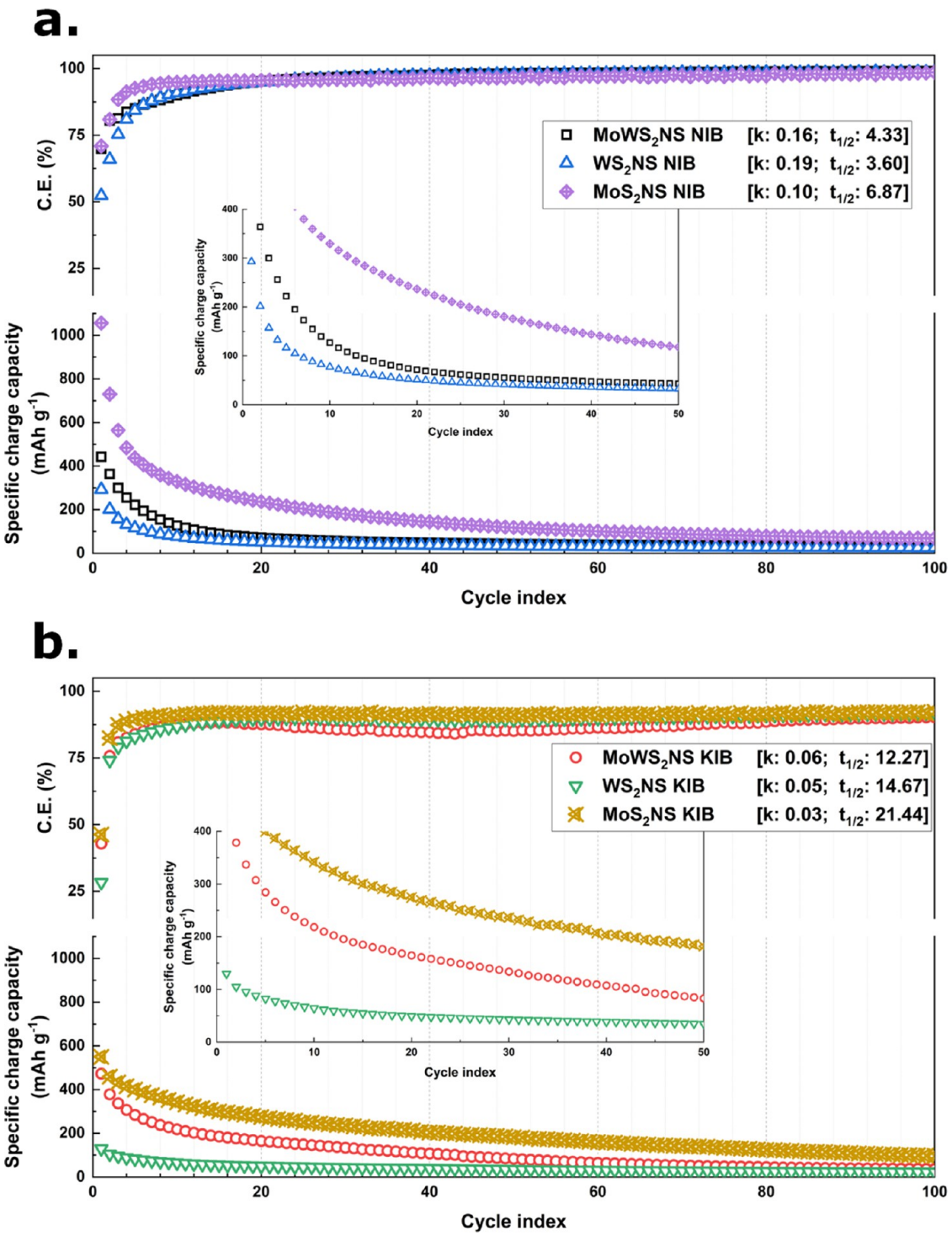


**Figure 5.** Cycling stability test and corresponding Coulombic efficiency of $MoS_2$, $WS_2$, and $MoWS_2$ electrodes in (a) Na-ion half-cells and (b) K-ion half-cells, along with rate constant ($k$) and half-life values ($t_{1/2}$) determined by exponential decay fitting.

regions, potentially due to the K-ion interaction with both $MoS_2$ and $WS_2$ lattices within the $MoWS_2$ alloy. The small and broad peak at 0.69 V was only attributed to $K^+$ reacting with $WS_2$. Compared to the first cycle, the second-cycle potassiation/depotassiation process demonstrated less intense peaks at the 0.71/1.38 and 1.04/1.61 V regions.

Figure 5 shows the long-term stability of all three neat electrodes in Na- and K-ion half-cell systems. During $Na^+$ storage, in Figure 5a, the $MoS_2$ electrode demonstrated the highest specific charge capacity of 1056 mAh $g^{-1}$, followed by $MoWS_2$ (442 mAh $g^{-1}$) and $WS_2$ (293 mAh $g^{-1}$). A similar trend was also observed for the first-cycle Coulombic efficiency ($MoS_2$: 71% > $MoWS_2$: 70% > $WS_2$: 52%). The low first-cycle Coulombic efficiency correlated well with the irreversible reactions observed during the sodiation step or SEI layer formation. All three cells showed gradual capacity fading behavior beginning in the second cycle, but, after repeated rigorous sodiation/desodiation cycles for 100 cycles, the $MoS_2$ electrode demonstrated the highest specific charge capacity (68 mAh $g^{-1}$), followed by $MoWS_2$ (32 mAh $g^{-1}$) and $WS_2$


https://doi.org/10.1021/acsomega.4c01966
ACS Omega 2024, 9, 24933−24947

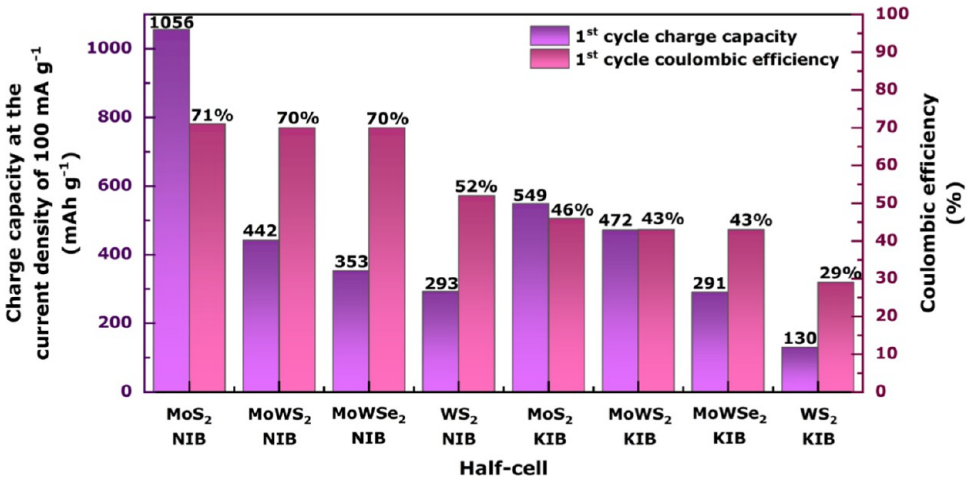


**Figure 6.** First-cycle charge capacity and Coulombic efficiency comparison between all of the half-cells of this study and the $MoWSe_2$ NIB and KIB from another study reported in ref 48

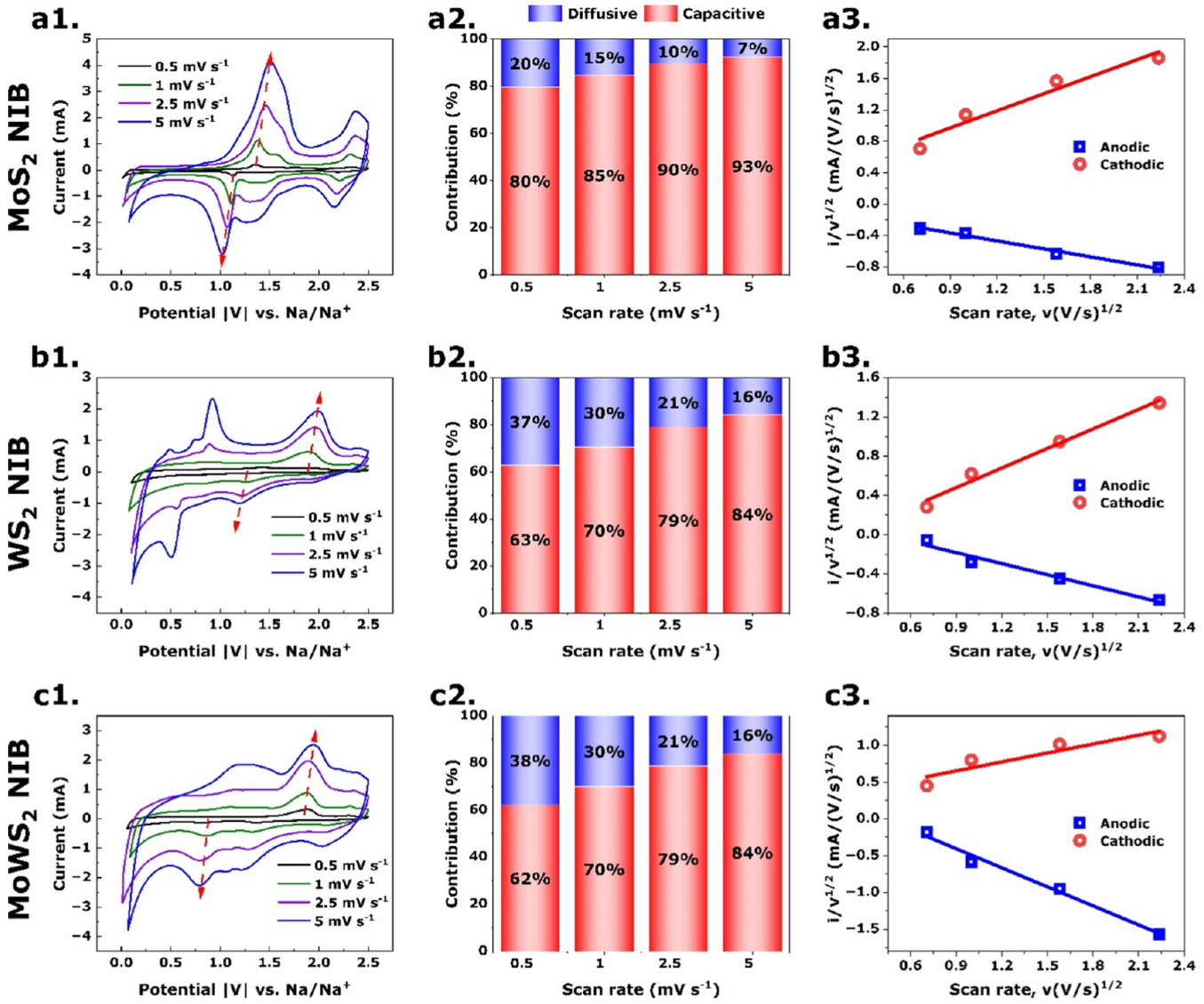


**Figure 7.** (a1) CV, (a2) capacitive vs diffusive contribution, (a3) fitting of anodic and cathodic voltammetric sweep data for $MoS_2$ NIB; (b1) CV, (b2) capacitive vs diffusive contribution, (b3) fitting of anodic and cathodic voltammetric sweep data for $WS_2$ NIB; (c1) CV, (c2) capacitive vs diffusive contribution, and (c3) fitting of anodic and cathodic voltammetric sweep data for $MoWS_2$ NIB.



https://doi.org/10.1021/acsomega.4c01966
ACS Omega 2024, 9, 24933−24947

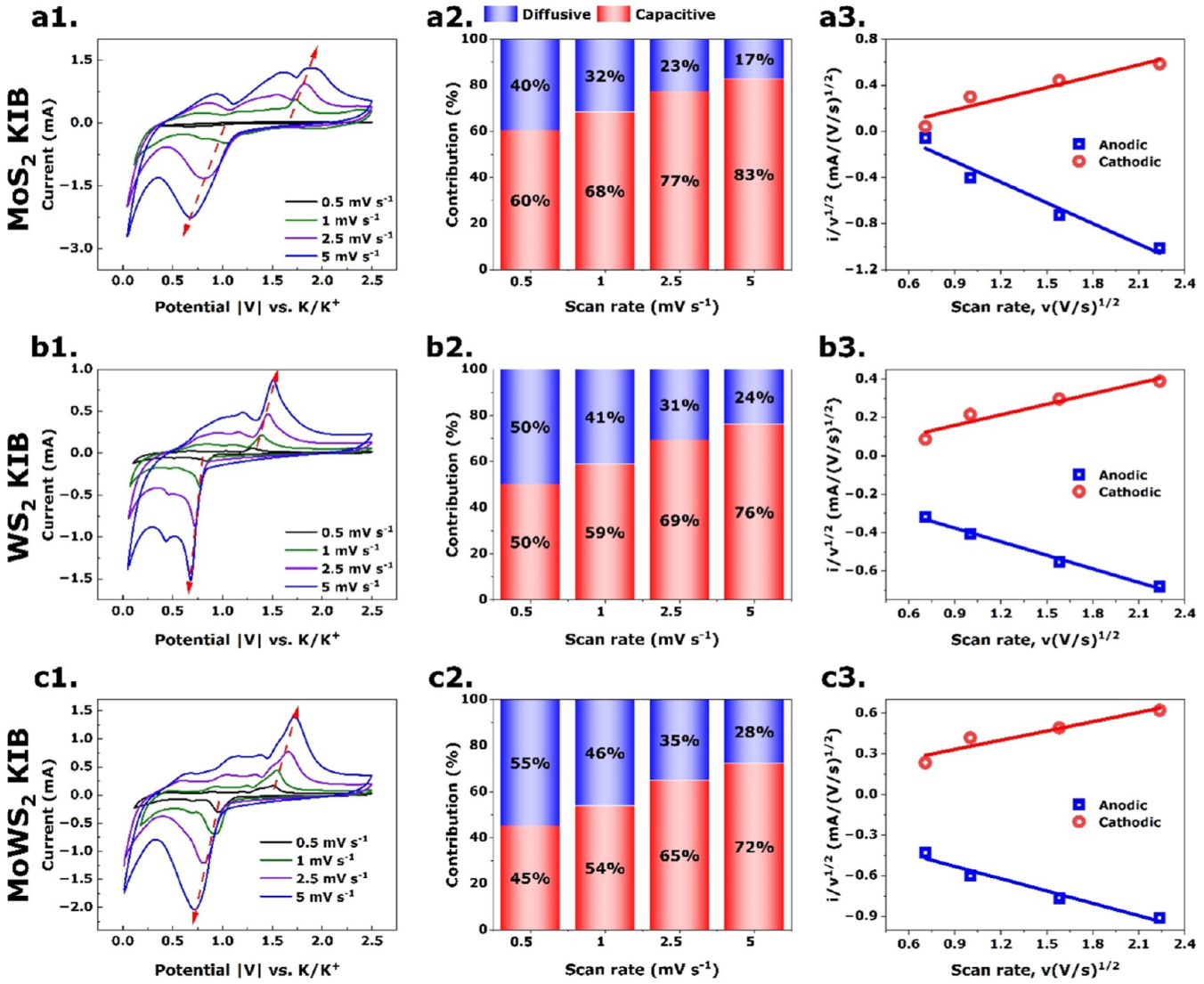


**Figure 8.** (a1) CV, (a2) capacitive vs diffusive contribution, and (a3) fitting of anodic and cathodic voltammetric sweep data for $MoS_2$ KIB; (b1) CV, (b2) capacitive vs diffusive contribution, and (b3) fitting of anodic and cathodic voltammetric sweep data for $WS_2$ KIB; and (c1) CV, (c2) capacitive vs diffusive contribution, and (c3) fitting of anodic and cathodic voltammetric sweep data for $MoWS_2$ KIB.

(25 mAh $g^{-1}$). The capacity values are lower compared to other research involving electrodes from high-surface-area TMD nanosheets or conducting TMD nanohybrids with carbon,[49,68−70] which are typically synthesized via bottom-up or wet-chemical synthesis. This expected discrepancy in the values is present because bulk or as-received TMD materials were used for the present work without nanostructuring.[29,71] The performance comparisons with different synthesis processes and this work are presented in Table S1.

Compared with Na-ion storage, all three materials demonstrated lower K-ion storage (Figure 5b). However, much like NIBs, $MoS_2$ possessed the highest specific charge capacity (549 mAh $g^{-1}$), followed by $MoWS_2$ (472 mAh $g^{-1}$) and $WS_2$ (130 mAh $g^{-1}$). The first-cycle Coulombic efficiency for all three electrodes followed a similar trend ($MoS_2$: 46% > $MoWS_2$: 43% > $WS_2$: 29%), but the first-cycle Coulombic efficiency of the KIB cells was much lower than the NIBs. The specific charge capacities of all three cells gradually faded from the second cycle. After continuous cycling for 100 potassiation/depotassiation steps, $MoS_2$ had the highest capacity (96 mAh $g^{-1}$), followed by $MoWS_2$ (36 mAh $g^{-1}$) and $WS_2$ (22 mAh $g^{-1}$).

The specific charge capacity plot was fitted with the following equation of the exponential decay function

$$y = y_0 + A_1 e^{-x/t_1} \quad (1)$$

where $y_0$ is offset, $A_1$ is amplitude, and $t_1$ is time constant. Parameters such as half-life ($t_{1/2}$) and decay constant ($k$) were also evaluated by using the nonlinear fit. The half-life refers to the duration it takes for half of the initial charge capacity to decay or transform. The shorter the half-life, the faster the exponential decay occurs. The $t_{1/2}$ of the performance of a half-cell can be determined using the following equation[72,73]

$$t_{1/2} = \frac{\ln 2}{k} \quad (2)$$

Here, $k$ measures the rate of decay, which is constant throughout the decay process for a given half-cell. In Na-ion storage (Figure 5a), the $MoS_2$ electrode exhibited the lowest decay constant ($k$ = $MoS_2$: 0.10 < $MoWS_2$: 0.16 < $WS_2$: 0.19)


https://doi.org/10.1021/acsomega.4c01966
ACS Omega 2024, 9, 24933−24947

and highest half-life ($t_{1/2}$ = $MoS_2$: 6.87 > $MoWS_2$: 4.33 > $WS_2$: 3.60). However, K-ion storage showed a similar result for the $MoS_2$ electrode (Figure 5b), including the lowest decay constant ($k$ = $MoS_2$: 0.03 < $WS_2$: 0.05 < $MoWS_2$: 0.06) and highest half-life ($t_{1/2}$ = $MoS_2$: 21.44 > $WS_2$: 14.67 > $MoWS_2$: 12.27) and $MoWS_2$ exhibited the lowest half-life among the KIB half-cells.

A comparison of these data with a previous study of $MoWSe_2$ TMD[48] (Figure 6) showed that, for both Na-ion and K-ion storage, the presence of molybdenum and its ratio in the TMD alloy most significantly affected charge capacity and capacity retention. A larger atomic (covalent) radius of tungsten (1.50 Å) compared to that of molybdenum (1.46 Å) was shown to potentially limit the intercalation of sodium and potassium ions.[74,75] Therefore, $WS_2$ exhibited the lowest charge capacity (NIB: 293 mAh $g^{-1}$ and KIB: 130 mAh $g^{-1}$) and lowest capacity retention (NIB: 52% and KIB: 29%). However, the inclusion of molybdenum increased the intercalation capacity, which led to higher charge capacity (NIB: 442 mAh $g^{-1}$ and KIB: 472 mAh $g^{-1}$) and higher cyclic efficiency (NIB: 70% and KIB: 43%) for $MoWS_2$ electrodes. Also, selenium (covalent radius of 1.18 Å) instead of sulfur (covalent radius of 1.04 Å) mitigated the reaction between TMDs and alkali ions due to its larger size.[74] Consequently, the $MoWSe_2$ NIB demonstrated a 353 mAh $g^{-1}$ charge capacity, while the $MoWSe_2$ KIB half-cell exhibited only 291 mAh $g^{-1}$. Both $MoWS_2$ and $MoWSe_2$ TMD alloys revealed very similar capacity retention for the first cycle, but only molybdenum and sulfur ($MoS_2$) electrodes provided the highest charge capacity (NIB: 1056 mAh $g^{-1}$ and KIB: 549 mAh $g^{-1}$) and superior capacity retention (NIB: 71% and KIB: 46%).

This study conducted cyclic voltammetry (CV) experiments at different scan rates to determine the fast physical charge storage mechanism within the anode material of $MoWS_2$ and further compared it to the base material.[76] Because the charge storage process utilizes different scan rates in CV experiments, with a varied current response due to different voltage sweeps, CV tests were performed at three scan rates (1, 2.5, and 5 mV $s^{-1}$) to study the sodium- and potassium-ion storage mechanisms of $MoS_2$, $WS_2$, and $MoWS_2$ for NIBs and KIBs.

Figure 7a1 shows CV plots obtained at the zeroth cycle for $MoS_2$ NIB half-cells at four scan rates (0.5, 1, 2.5, and 5 mV $s^{-1}$) to evaluate the interaction of $Na^+$ with the $MoS_2$ active material. Clear and distinguishable peaks were observed at 1.11, 1.42, and 2.22 V during the sodiation process and 2.32, 1.58, and 1.38 V during the desodiation process at a scan rate of 1 mV $s^{-1}$ in the zeroth cycle. These peaks were analogous to peaks from the differential capacity curves from the second cycle onward. Although the sodiation peaks move to lower voltages, at higher scan rates of 2.5 and 5 mV $s^{-1}$, the desodiation peaks also moved to higher voltages. Also, at a lower scan rate of 0.5 mV $s^{-1}$, the peaks shift to higher or lower voltages during the sodiation and desodiation processes, respectively.

The CV plots at four scan rates are shown in Figure 7b1 for the $WS_2$ NIB cells. The CV plot at 1 mV $s^{-1}$ in Figure 7b1 demonstrates pronounced peaks at 0.6, 1.25, and 1.9 V during sodiation and 0.4, 0.7, 0.9, and 1.9 V during the desodiation process. At higher scan rates, the sodiation peaks shifted to lower voltages, and the desodiation peaks moved to higher voltages, and at a lower scan rate, the peaks shifted in the opposite direction.

The CV plots of the $MoWS_2$ electrode in the NIB half-cell system are shown in Figure 7c1. Similar to the differential capacity curves, the 1 mV $s^{-1}$ curve before cycling demonstrated $MoS_2$ peaks at 2.2, 1.3, and 1.1 V and WS2 peaks at 0.8 V during sodiation. During desodiation for the same scan rate, $MoS_2$ showed peaks at 2.3 and 1.3 V and $WS_2$ showed peaks at 0.4 and 1.9 V before cycling. These peaks shifted at lower and higher scan rates of 0.5, 2.5, and 5 mV $s^{-1}$.

Similarly, CV plots in Figure 8a1 show peaks for $MoS_2$ KIB at 1.98, 1.05, and 0.78 V during potassiation and 0.4, 0.78, 1.46, and 1.7 V during the depotassiation process at a scan rate of 1 mV $s^{-1}$ at the zeroth cycle. Like NIBs, the potassiation peaks shifted to lower voltages, while the depotassiation peaks moved to higher voltages at higher scan rates in the CV plots obtained before cycling. At a slower scan rate of 0.5 mV $s^{-1}$, the intensity of the peaks is also low. The new peaks in the CV plots could be due to a slow scan rate, which allowed $K^+$-ions more time to participate in different reactions.

CV plots for $WS_2$ KIB electrodes are shown in Figure 8b1 at four scan rates (0.5, 1, 2.5, and 5 mV $s^{-1}$). In the CV plot before cycling, peaks were visible at 1.1 and 1.4 V during depotassiation and only one broad feature was visible at 0.78 V during potassiation at 1 mV $s^{-1}$. Nevertheless, all of the peaks shifted to lower/higher voltages during potassiation/depotassiation at higher scan rates of 2.5 and 5 mV $s^{-1}$, respectively, and shifted to the opposite direction at a lower scan rate of 0.5 mV $s^{-1}$.

Figure 8c1 shows CV plots at various scan rates for $MoWS_2$ KIB electrodes before cycling. At a slower scan rate of 1 mV $s^{-1}$, $MoS_2$-like 1.0 V and $WS_2$-like 0.7 V peaks were present during the potassiation process before cycling the cell, while the depotassiation process contained $MoS_2$-like peaks at 0.4 and 0.9 V and $WS_2$-like peaks at 1.2 and 1.6 V. Similar to other electrodes, these peaks shifted slightly at higher and lower scan rates.

CV plots were further analyzed to estimate the proportion of surface capacitive effects and diffusion-controlled insertion process.[77,78] Equation 3 translates the total sum of the contributions

$$\frac{i(V)}{\nu^{1/2}} = k_1\nu^{1/2} + k_2 \tag{3}$$

where $k_1\nu^{1/2}$ is the contribution from surface capacitive effects and $k_2$ corresponds to the diffusion-controlled intercalation mechanism. From the CV plots, the proportion of contribution was calculated for the zeroth cycle for six cells. The capacity contributions for $MoS_2$, $WS_2$, and $MoWS_2$ electrodes in NIB and KIB systems are illustrated in Figures 7a2−c2 and 8a2−c2. As shown, the capacitive contribution increased with an increase in scan rate. The diffusive contributions for the $MoS_2$ NIB cell were 20, 15, 10, and 7% in the zeroth cycle at scan rates of 0.5, 1, 2.5, and 5 mV $s^{-1}$, respectively, while the diffusive contributions for the $MoS_2$ KIB cell were 40, 32, 23, and 17% in the zeroth cycle at the same scan rates. Similarly, the diffusive contributions were 37, 30, 21, and 16% for the $WS_2$ NIB cell and 50, 41, 31, and 24% for the $WS_2$ KIB cell in the zeroth cycle at the scan rates of 0.5, 1, 2.5, and 5 mV $s^{-1}$, respectively. Correspondingly, for the $MoWS_2$ NIB cells, the diffusive contributions were 38, 30, 21, and 16% in the zeroth cycle, and for the $MoWS_2$ KIB cells, the diffusive contributions were 55, 46, 35, and 28% in the zeroth cycle at the scan rates of 0.5, 1, 2.5, and 5 mV $s^{-1}$, respectively. According to the capacity contribution plots, $MoWS_2$ shows


https://doi.org/10.1021/acsomega.4c01966
ACS Omega 2024, 9, 24933−24947

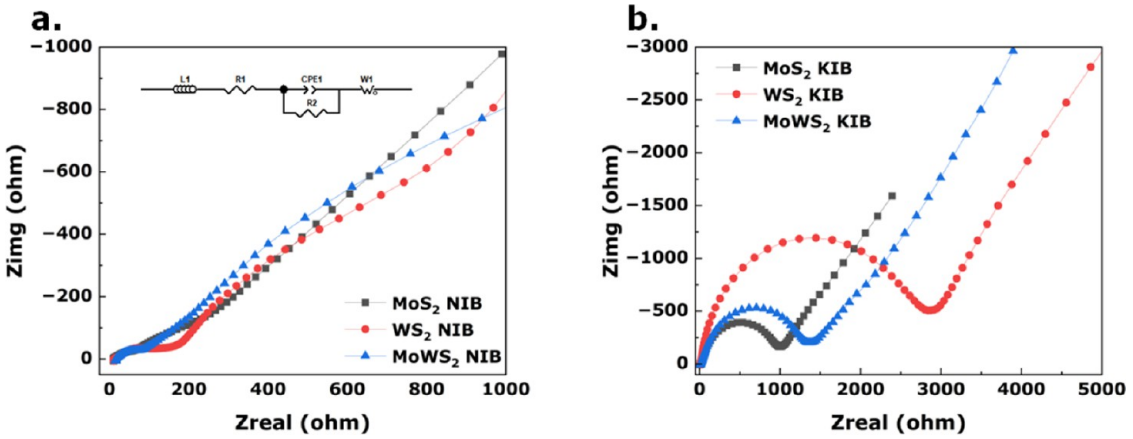


**Figure 9.** Nyquist plot at the 11th cycle for $MoS_2$, $WS_2$, and $MoWS_2$ electrodes in (a) Na-ion half-cells and (b) K-ion half-cells (electrode area = 1.6 $cm^2$).

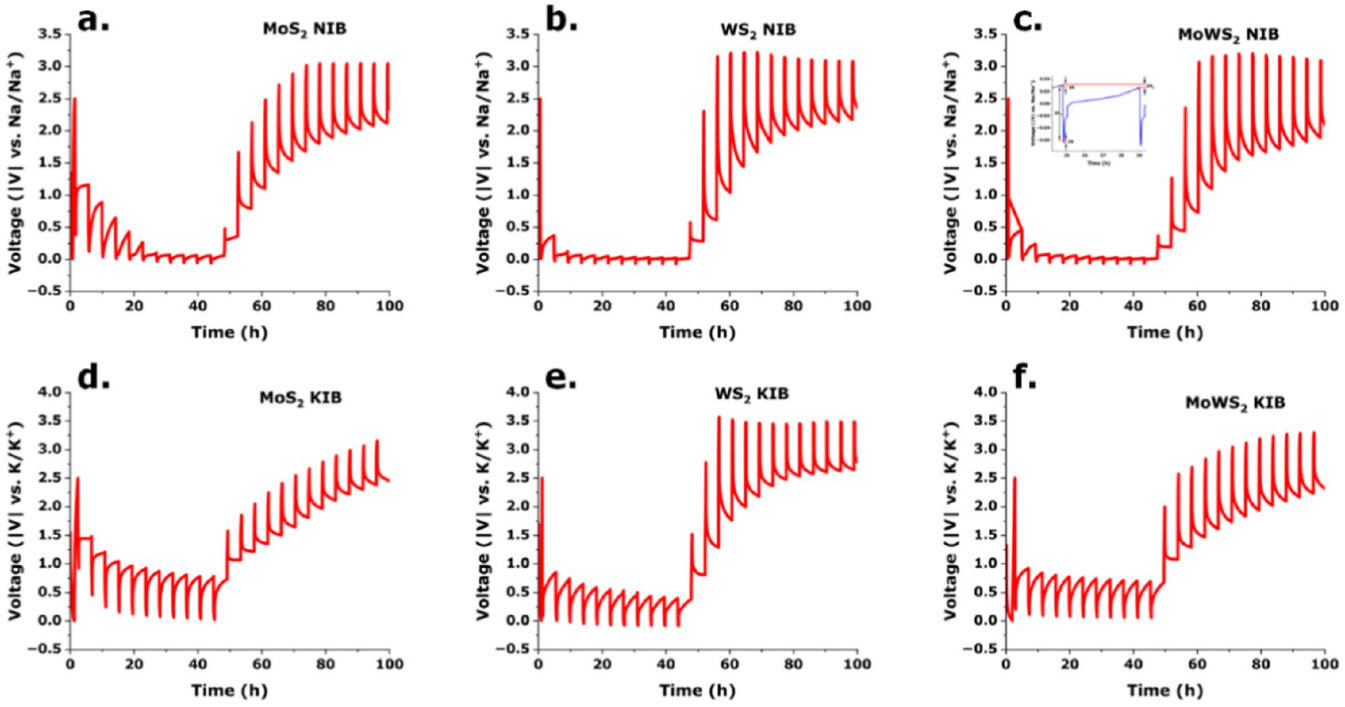


**Figure 10.** Charge and discharge cycles with 15 min of current pulse at a 100 mA $g^{-1}$ electrode followed by 12 h of relaxation for (a) $MoS_2$ NIB, (b) $WS_2$ NIB, (c) $MoWS_2$ NIB, (d) $MoS_2$ KIB, (e) $WS_2$ KIB, and (f) $MoWS_2$ KIB.

the highest diffusive behavior compared to $MoS_2$ and $WS_2$ for both NIBs and KIBs.

Figures 7a3−c3 and8a3−c3 show the fitting of anodic and cathodic voltammetric sweep data for the electrodes for scan rates at 0.5, 1, 2.5, and 7.5 mV $s^{-1}$. This linear behavior, which is also related to eq 3, allows the calculation of constant values $k_1$ and $k_2$.

This study analyzed electrochemical impedance spectroscopy (EIS) data to investigate the kinetic behavior of as-obtained TMDs and TMD alloy electrodes. EIS measurements were obtained after discharging the cells at the 11th cycle, after ensuring complete relaxation of the half-cells and reaching the open-circuit voltage of 0.1 V.

The Nyquist plots of all of the NIB and KIB half-cells showed an inductive loop in the high-frequency stage, which was attributed to the measurement system (wiring to the half-cell) or the cell geometry and windings. The high-frequency intercept of the real impedance axis common to all of the cells corresponded to the sum of internal Ohmic resistance ($R_{ohm}$), which arises from the electrolyte, active material, current collectors, and electrical contacts. Figure 9 shows a typical semicircular curve in the high-frequency zone in the Nyquist plots of all of the NIB and KIB cells, and the low-frequency zone consists of a diagonal straight line. The area of the semicircles indicates impedance caused by the charge transfer between the electrolyte and the electrode interface. The contact impedance between the electrode interface and electrolyte decreased with a smaller radius.[79,80] Because the SEI formation could not be differentiated from the charge transfer, it was fitted with $CPE_{dl}$ and $R_{CT}$ elements in parallel. The low-frequency stage of the Nyquist plots showed a sloping line or long tail fitted with a Warburg element to reflect the solid-state diffusion. The fitted $W-P$ values always deviated from an ideal condition, indicating the existence of other


https://doi.org/10.1021/acsomega.4c01966
ACS Omega 2024, 9, 24933−24947

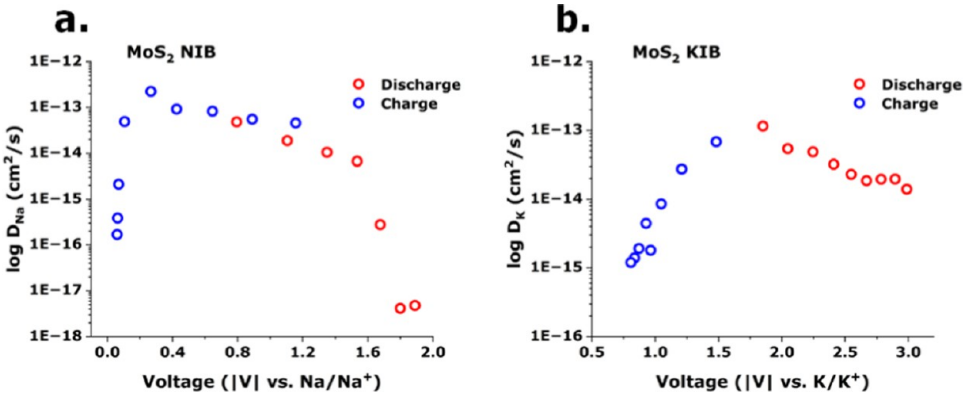


**Figure 11.** Diffusion coefficients as a function of discharge and charge for $MoS_2$: (a) NIB and (b) KIB half-cells.

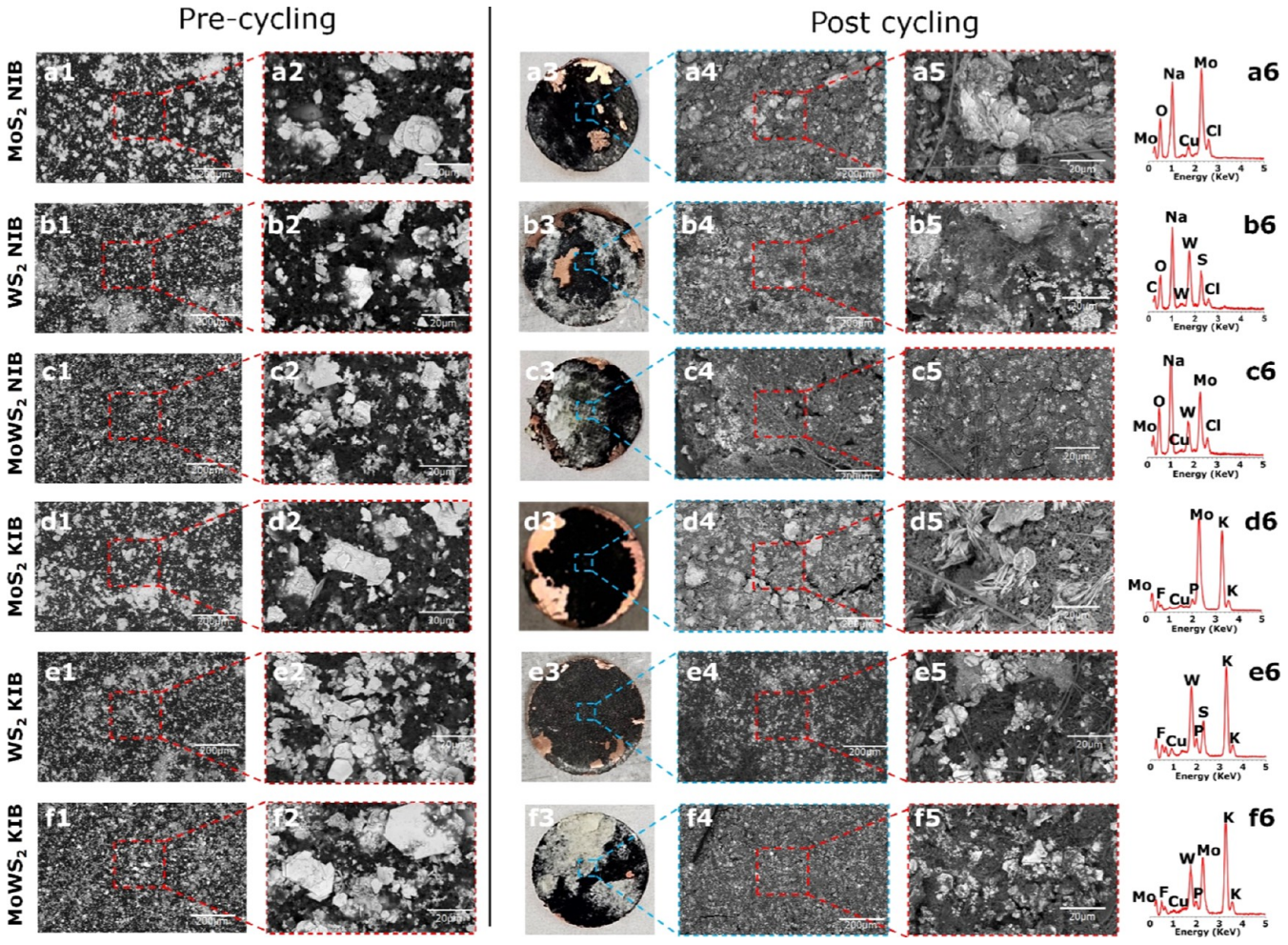


**Figure 12.** (a1, a2−f1, f2) SEM micrographs of pristine electrodes indicating structural integrity before cycling, (a3−f3) digital camera image of the cycled electrodes, (a4, a5−f4, f5) SEM micrographs of cycled electrodes, and (a6−f6) XRF spectra of the electrodes to identify the elemental composition.

processes besides solid-state diffusion, such as migration and liquid/electrolyte phase diffusion.[8]

The Nyquist plots in Figure 9a for NIBs and Figure 9b for KIBs were fitted with an equivalent circuit using Zview software (version 3.2b, Copyright Scribner Associates, Inc., Southern Pines, NC). The obtained fitted data are shown in Tables S2 and S3, and the equivalent circuit is illustrated in inset of Figure 9a. The tabulated values of charge-transfer resistance ($R_{CT}$) revealed that $MoS_2$ cells have the lowest resistance (10.08 for NIB and 967.5 for KIB). Although the $WS_2$ cells exhibited the highest charge-transfer resistance ($R_{CT}$ = 149.9 for NIB and 2211 for KIB), the $R_{CT}$ is much higher for KIBs than NIBs (i.e., $R_{CT}$ for $MoWS_2$ NIB = 51.38; $R_{CT}$ for $MoWS_2$ KIB = 1001).

To determine the change in potential over time, this study utilized the galvanostatic intermittent titration technique (GITT) (Figure 10) by charging/discharging at a 100 mAh $g^{-1}$ current pulse for 15 min, followed by 12 h of relaxation


https://doi.org/10.1021/acsomega.4c01966
ACS Omega 2024, 9, 24933−24947

between pulses. During the relaxation period, the magnitude of voltage increased in the insertion process and decreased in the extraction process.[81] The diffusion coefficient for $Na^+$ and $K^+$ was determined using the equation 4[60]

$$D_{Na^+} = \frac{4}{\pi\tau}\left(\frac{n_m V_m}{S}\right)^2\left(\frac{\Delta E_s}{\Delta E_\tau}\right)^2 \quad (4)$$

where $\tau$ is the duration of the current pulse, which is 15 min or 900 s; $n_m$ is the mole number (for $MoS_2$ NIB: $4.46 \times 10^{-6}$ mol and for KIB: $5.31 \times 10^{-6}$ mol); $V_m$ is the molar volume (for $MoS_2$: 31.65 $cm^3\ mol^{-1}$); $S$ is the total contacting area between the electrode and electrolyte (1.6 $cm^2$); $\Delta E_s$ is the voltage change between two adjacent equilibrium states; and $\Delta E_\tau$ is the voltage change induced by the galvanostatic charge/discharge, shown in the inset of Figure 10c. This study showed diffusion coefficient plots for only the $MoS_2$ electrodes, as they showed higher capacity and a consistent trend compared to others.

Figure 11a represents the sodium diffusion coefficients ($D_{Na}$), and Figure 11b represents the potassium diffusion coefficients ($D_K$) as a function of voltage during charging and discharging for the $MoS_2$ half-cell. The $MoS_2$ NIB half-cell exhibited a $D_{Na}$ of $\approx 10^{-16}$–$10^{-13}$ $cm^2\ s^{-1}$ during charge and $\approx 10^{-18}$–$10^{-13}$ $cm^2\ s^{-1}$ during discharge, which is correlated with previous studies.[82,83] Furthermore, $D_K$ of $\approx 10^{-15}$–$10^{-13}$ $cm^2\ s^{-1}$ during charge and $\approx 10^{-14}$–$10^{-13}$ $cm^2\ s^{-1}$ during discharge were observed for the $MoS_2$ KIB half-cells, which is identical to previous works.[84−86] Additionally, during the charging state, the $D_{Na}$ for $WS_2$ and $MoWS_2$ were $\approx 10^{-14}$–$10^{-11}$ and $\approx 10^{-14}$–$10^{-13}$ $cm^2\ s^{-1}$, respectively, and during the discharging state, the $D_{Na}$ for both were $\approx 10^{-15}$–$10^{-12}$ $cm^2\ s^{-1}$. On the other hand, during the charging state, the $D_K$ for $WS_2$ and $MoWS_2$ were $\approx 10^{-14}$–$10^{-13}$ and $\approx 10^{-15}$–$10^{-14}$ $cm^2\ s^{-1}$, respectively, and during the discharging state, the $D_K$ for $WS_2$ were $\approx 10^{-15}$ $cm^2\ s^{-1}$ and $D_K$ for $MoWS_2$ was $\approx 10^{-15}$–$10^{-14}$ $cm^2\ s^{-1}$.

The SEM images in Figure 12a1,a2-f1,f2 show a uniform distribution of TMD and TMD alloy nanosheets when mixed with a conductive agent and binder before cycling in the electrode format. The digital camera images (Figure 12a3−f3) were visually inspected to compare the conditions of the neat electrodes with electrodes after prolonged cycling. No imperfection or discoloration of the electrodes was visible. However, some electrodes peeled off during disassembly (Figure 12b3 for $WS_2$ NIB and Figure 12d3 for $MoS_2$ KIB). After further inspection via SEM, the white substances on top of the electrode seemed to originate from the attached fiber of the separator (Figure 12a5,c5,e5).

Figure 12a4,a5−c4,c5 shows that the geometrical characteristics and uniform dispersion of TMD particles were not present for NIBs after the long cycling process (Figure 12a1,a2−c1,c2). However, some TMD particles with smooth geometrical shapes remain visible in Figure 12d4,d5-f4,f5 for the KIB cells. The smaller Na-ions may have intercalated into almost all of the TMD particles, but the larger K-ions could only introduce themselves to the surface of the large TMD flakes. Consequently, almost all of the TMD flakes in the NIB cells were broken into irregular smaller particles, while the large TMD flakes in the KIB cells were in mint condition after cycling.

As shown in Figure 12a4−f4, few cracks were observed in the electrodes at low magnifications, while surface cracks in the NIB and KIB electrodes ($MoS_2$, $WS_2$, and $MoWS_2$) were visible at high magnification (Figure 12a5−f5). However, the surface cracks could be a result of drying the dissembled electrodes on the hot plate at 80 °C for 24 h, resulting in a severe change in volume.

X-ray fluorescence (XRF) of the cycled electrodes demonstrated qualitative elemental analysis, with peaks for Mo, W, and S representing elemental existence after cycling (Figure 12a6−f6). Due to the electrolyte, Na, Cl, and O peaks were observed in all of the NIB half-cells, and K, P, and F peaks were observed in all of the KIB half-cells. Peaks of Cu were detected due to electrode preparation on Cu foil. The elemental compositions of all of the Na-ion and K-ion cells collected from XRF spectra are listed in Table S4.

## CONCLUSIONS

In summary, the electrochemical cycling of Na-ion and K-ions in TMDs ($MoS_2$ and $WS_2$) and TMD alloy ($MoWS_2$ and $MoWSe_2$) nanoflakes was studied and compared for possible use as high capacity electrodes in NIB and KIBs. At the potential range of 0.01−2.5 V, the $MoS_2$ electrode demonstrated the highest $Na^+$ charge capacity (1056 mAh $g^{-1}$) and the best first cycle Coulombic efficiency (71%). The $MoS_2$ electrode also showed the highest $K^+$ charge capacity (549 mAh $g^{-1}$) and the best retention capacity (46%) among the KIB half-cells. The fitted cyclic stability plot indicated that Na-ion and K-ion half-cells with $MoS_2$ electrodes possess the highest half-life (NIB: 6.87; KIB: 21.43) compared to other TMD electrodes. The size of the individual constituent atoms (Mo, W, S, Se) plays a critical role in the alkali-metal ion intercalation process in TMDs. With the increase in size of the metal-ion, specific capacity and Coulombic efficiency decreased correspondingly.. Based on postcycling analysis almost all of the large flakes of TMDs have participated in the $Na^+$ reaction process and nearly all of the large flakes disintergrated into smaller particles. However, for KIBs, the large TMD flakes were obtained almost in pristine condition after even a long cycling process, which indicated the lack of $K^+$ intercalation and conversion reactions in larger TMD flakes. Also, the CV and capacitive contribution plots imply that combining tungsten and molybdenum (as in alloy TMD) shows increased diffusive contribution compared to the neat TMDs (the highest diffusive contribution observed at 1 mV $s^{-1}$). It is likely that the superior performance of $MoS_2$ compared to other TMDs and TMD alloys is due to the mismatched crystal structure or large elemental size of the tungsten atom. The electrochemical impedance study further demonstrated that the TMDs with only molybdenum and sulfur ($MoS_2$) have the lowest electrical resistance between the electrolyte and electrode. In contrast, the resistance for the TMD alloy with both tungsten and molybdenum ($MoWS_2$) or tungsten ($WS_2$) was comparatively higher. This study established the foundation for future investigation of TMD and TMD alloybased electrodes in emerging electrochemical energy storage devices.

## ASSOCIATED CONTENT

### Supporting Information

The Supporting Information is available free of charge at https://pubs.acs.org/doi/10.1021/acsomega.4c01966.

Data for electrochemical performance comparison of $MoS_2$ and $WS_2$ NIBs and KIBs with different synthesis



https://doi.org/10.1021/acsomega.4c01966
ACS Omega 2024, 9, 24933−24947

processes and this work (Table S1), circuit-fitted results from EIS experiments for NIBs (Table S2), circuit-fitted results from EIS experiments for KIBs (Table S3), and cycling elemental composition of the spent half-cell electrodes determined by XRF (Table S4) (PDF)

## AUTHOR INFORMATION


### Corresponding Authors

**Arijit Roy** − *Mechanical and Nuclear Engineering, Kansas State University, Manhattan, Kansas 66506-0100, United States;* orcid.org/0009-0004-8026-2330; Email: arijit@ksu.edu

**Gurpreet Singh** − *Mechanical and Nuclear Engineering, Kansas State University, Manhattan, Kansas 66506-0100, United States;* orcid.org/0000-0003-2126-9204; Email: gurpreet@ksu.edu

### Author

**Sonjoy Dey** − *Mechanical and Nuclear Engineering, Kansas State University, Manhattan, Kansas 66506-0100, United States;* orcid.org/0000-0001-6244-2750

Complete contact information is available at: https://pubs.acs.org/10.1021/acsomega.4c01966


### Author Contributions

Conceptualization: G.S.; methodology: G.S., A.R., and S.D.; $MoS_2$, $MoWS_2$, and $WS_2$ syntheses and TEM analysis: S.D.; XPS, XRD, XRF, and Raman: A.R. and S.D.; cell assembly and data acquisition: A.R.; GCD, CV, and differential capacity: A.R. and S.D.; postcycling analysis: A.R.; resources: G.S.; data curation: A.R.; writing—original draft preparation: A.R. and S.D.; writing—review and editing: G.S.; visualization: A.R.; supervision: G.S.; and funding acquisition: G.S. All authors have read and agreed to the published version of the manuscript.

### Notes

The authors declare no competing financial interest.

## ACKNOWLEDGMENTS

This work is supported by the National Science Foundation grants #1743701, 1454151, and 2025298. The research was performed, in part, in the Nebraska Nanoscale Facility: National Nanotechnology Coordinated Infrastructure and the Nebraska Center for Materials and Nanoscience (and/or NERCF), which are supported by the National Science Foundation under Award ECCS: 2025298, and the Nebraska Research Initiative. The authors extend their gratitude to Dr. Shakir Bin Mujib for his guidance in SEM, Raman, XRD, and XRF analyses, as well as his advice on data presentation.

## REFERENCES


(1) Ryu, M.; Hong, Y.-K.; Lee, S.-Y.; Park, J. H. Ultrahigh loading dry-process for solvent-free lithium-ion battery electrode fabrication. *Nat. Commun.* **2023**, *14* (1), No. 1316.

(2) Tan, D. H. S.; Banerjee, A.; Chen, Z.; Meng, Y. S. From nanoscale interface characterization to sustainable energy storage using all-solid-state batteries. *Nat. Nanotechnol.* **2020**, *15* (3), 170−180.

(3) Zhang, W.; Liu, Y.; Guo, Z. Approaching high-performance potassium-ion batteries via advanced design strategies and engineering. *Sci. Adv.* **2019**, *5* (5), No. eaav7412, DOI: 10.1126/sciadv.aav7412.

(4) Zhang, W.; Lu, J.; Guo, Z. Challenges and future perspectives on sodium and potassium ion batteries for grid-scale energy storage. *Mater. Today* **2021**, *50*, 400−417.

(5) Tarascon, J. M.; Armand, M. Issues and challenges facing rechargeable lithium batteries. *Nature* **2001**, *414* (6861), 359−367.

(6) Zheng, P.; Liu, T.; Guo, S. Micro-nano structure hard carbon as a high performance anode material for sodium-ion batteries. *Sci. Rep.* **2016**, *6* (1), No. 35620, DOI: 10.1038/srep35620.

(7) Larcher, D.; Tarascon, J. M. Towards greener and more sustainable batteries for electrical energy storage. *Nat. Chem.* **2015**, *7* (1), 19−29.

(8) Dey, S.; Singh, G. Differentiating Cyclability and Kinetics of Na+ Ions in Surface-Functionalized and Nanostructured Graphite Using Electrochemical Impedance Spectroscopy. *Batteries* **2023**, *9*, No. 534, DOI: 10.3390/batteries9110534.

(9) Hu, Y.; Ding, H.; Bai, Y.; Liu, Z.; Chen, S.; Wu, Y.; Yu, X.; Fan, L.; Lu, B. Rational Design of a Polyimide Cathode for a Stable and High-Rate Potassium-Ion Battery. *ACS Appl. Mater. Interfaces* **2019**, *11* (45), 42078−42085.

(10) Moriwake, H.; Kuwabara, A.; Fisher, C. A.; Ikuhara, Y. Why is sodium-intercalated graphite unstable? *RSC Adv.* **2017**, *7* (58), 36550−36554.

(11) Jian, Z.; Luo, W.; Ji, X. Carbon Electrodes for K-Ion Batteries. *J. Am. Chem. Soc.* **2015**, *137* (36), 11566−11569.

(12) Kubota, K.; Dahbi, M.; Hosaka, T.; Kumakura, S.; Komaba, S. Towards K-Ion and Na-Ion Batteries as "Beyond Li-Ion. *Chem. Rec.* **2018**, *18* (4), 459−479.

(13) Rathnayake, R. M. N. M.; Duignan, T. T.; Searles, D. J.; Zhao, X. S. Exploring the effect of interlayer distance of expanded graphite for sodium ion storage using first principles calculations. *Phys. Chem. Chem. Phys.* **2021**, *23* (4), 3063−3070.

(14) Trano, S.; Versaci, D.; Castellino, M.; Fontana, M.; Fagiolari, L.; Francia, C.; Bella, F. Exploring nature-behaviour relationship of carbon black materials for potassium-ion battery electrodes. *Energy Mater.* **2024**, *4* (1), No. 400008.

(15) Shao, Y.; Yang, Q.; Zhang, Y.; Jiang, N.; Hao, Y.; Qu, K.; Du, Y.; Qi, J.; Li, Y.; Tang, Y.; Lu, X.; Zhang, L.; Qiu, J. A Universal Method for Regulating Carbon Microcrystalline Structure for High-Capacity Sodium Storage: Binding Energy As Descriptor. *ACS Nano* **2023**, *17* (23), 24012−24021.

(16) Wang, F.; Zhang, T.; Zhang, T.; He, T.; Ran, F. Recent Progress in Improving Rate Performance of Cellulose-Derived Carbon Materials for Sodium-Ion Batteries. *Nano-Micro Lett.* **2024**, *16* (1), No. 148, DOI: 10.1007/s40820-024-01351-2.

(17) Wang, J.; Liu, X.; Jia, H.; Apostol, P.; Guo, X.; Lucaccioni, F.; Zhang, X.; Zhu, Q.; Morari, C.; Gohy, J.-F.; Vlad, A. A High-Voltage Organic Framework for High-Performance Na- and K-Ion Batteries. *ACS Energy Lett.* **2022**, *7* (2), 668−674.

(18) Tanibata, N.; Nonaka, N.; Makino, K.; Takeda, H.; Nakayama, M. Chloride electrode composed of ubiquitous elements for high-energy-density all-solid-state sodium-ion batteries. *Sci. Rep.* **2024**, *14* (1), No. 2703.

(19) Tan, H.; Lin, X. Electrolyte Design Strategies for Non-Aqueous High-Voltage Potassium-Based Batteries. *Molecules* **2023**, *28*, No. 823, DOI: 10.3390/molecules28020823.

(20) Trano, S.; Corsini, F.; Pascuzzi, G.; Giove, E.; Fagiolari, L.; Amici, J.; Francia, C.; Turri, S.; Bodoardo, S.; Griffini, G.; Bella, F. Lignin as Polymer Electrolyte Precursor for Stable and Sustainable Potassium Batteries. *ChemSusChem* **2022**, *15* (12), No. e202200294.

(21) Gandolfo, M.; Amici, J.; Fagiolari, L.; Francia, C.; Bodoardo, S.; Bella, F. Designing photocured macromolecular matrices for stable potassium batteries. *Sustainable Mater. Technol.* **2022**, *34*, No. e00504.

(22) Chen, M.; Wu, J.; Ye, T.; Ye, J.; Zhao, C.; Bi, S.; Yan, J.; Mao, B.; Feng, G. Adding salt to expand voltage window of humid ionic liquids. *Nat. Commun.* **2020**, *11* (1), No. 5809.

(23) Zhang, Y.; Guo, X.; Yang, Q.; Shao, Y.; Du, Y.; Qi, J.; Zhao, M.; Shang, Z.; Hao, Y.; Tang, Y.; et al. Chemical and spatial dual-confinement engineering for stable Na-S batteries with approximately

100% capacity retention. *Proc. Natl. Acad. Sci. U.S.A.* **2023**, *120* (48), No. e2314408120.
(24) Shao, Y.; Cui, Y.; Wang, C.; Yang, Q.; Hong, S.; Tang, Y.; Zhang, Y.; Guo, X.; Zhang, L.; Song, L.; Qiu, J. Initiating Fluorine Chemistry in Polycyclic Aromatic Hydrocarbon-Derived Carbon for New Cluster-Mode Na Storage with Superhigh Capacity. *Small* **2023**, *19* (22), No. 2300107.
(25) Zhao, Z.; Gao, C.; Fan, J.; Shi, P.; Xu, Q.; Min, Y. Dual Confinement of CoSe2 Nanorods with Polyphosphazene-Derived Heteroatom-Doped Carbon and Reduced Graphene Oxide for Potassium-Ion Batteries. *ACS Omega* **2021**, *6* (26), 17113−17125.
(26) Chen, B.; Chao, D.; Liu, E.; Jaroniec, M.; Zhao, N.; Qiao, S.-Z. Transition metal dichalcogenides for alkali metal ion batteries: engineering strategies at the atomic level. *Energy Environ. Sci.* **2020**, *13* (4), 1096−1131.
(27) Cook, J. B.; Kim, H. S.; Yan, Y.; Ko, J. S.; Robbennolt, S.; Dunn, B.; Tolbert, S. H. Mesoporous MoS2 as a Transition Metal Dichalcogenide Exhibiting Pseudocapacitive Li and Na-Ion Charge Storage. *Adv. Energy Mater.* **2016**, *6* (9), No. 1501937, DOI: 10.1002/aenm.201501937.
(28) Ren, X. D.; Zhao, Q.; McCulloch, W. D.; Wu, Y. Y. MoS2 as a long-life host material for potassium ion intercalation. *Nano Res.* **2017**, *10* (4), 1313−1321.
(29) Dey, S.; Singh, G. WS2 Nanosheet Loaded Silicon-Oxycarbide Electrode for Sodium and Potassium Batteries. *Nanomaterials* **2022**, *12*, No. 4185, DOI: 10.3390/nano12234185.
(30) Fagiolari, L.; Versaci, D.; Di Berardino, F.; Amici, J.; Francia, C.; Bodoardo, S.; Bella, F. An Exploratory Study of MoS2 as Anode Material for Potassium Batteries. *Batteries* **2022**, *8*, No. 242, DOI: 10.3390/batteries8110242.
(31) Tang, L. B.; Zhang, B.; Peng, T.; He, Z. J.; Yan, C.; Mao, J.; Dai, K. H.; Wu, X. W.; Zheng, J. C. MoS2/SnS@C hollow hierarchical nanotubes as superior performance anode for sodium-ion batteries. *Nano Energy* **2021**, *90*, No. 106568, DOI: 10.1016/j.nanoen.2021.106568.
(32) Su, D. W.; Dou, S. X.; Wang, G. X. Ultrathin MoS2 Nanosheets as Anode Materials for Sodium-Ion Batteries with Superior Performance. *Adv. Energy Mater.* **2015**, *5* (6), No. 1401205, DOI: 10.1002/aenm.201401205.
(33) Hu, Z.; Wang, L. X.; Zhang, K.; Wang, J. B.; Cheng, F. Y.; Tao, Z. L.; Chen, J. MoS2 Nanoflowers with Expanded Interlayers as High-Performance Anodes for Sodium-Ion Batteries. *Angew. Chem., Int. Ed.* **2014**, *53* (47), 12794−12798.
(34) Fang, Y.; Luan, D.; Chen, Y.; Gao, S.; Lou, X. W. Rationally designed three-layered Cu2S@ Carbon@ MoS2 hierarchical nanoboxes for efficient sodium storage. *Angew. Chem.* **2020**, *132* (18), 7245−7250.
(35) Choi, S. H.; Ko, Y. N.; Lee, J. K.; Kang, Y. C. 3D MoS2−graphene microspheres consisting of multiple nanospheres with superior sodium ion storage properties. *Adv. Funct. Mater.* **2015**, *25* (12), 1780−1788.
(36) Dey, S.; Roy, A.; Mujib, S. B.; Krishnappa, M.; Zak, A.; Singh, G. Addressing Irreversibility and Structural Distortion in WS2 Inorganic Fullerene-Like Nanoparticles: Effects of Voltage Cutoff Experiments in Beyond Li+-Ion Storage Applications. *ACS Omega* **2024**, *9* (15), 17125−17136.
(37) Dey, S.; Manjunath, K.; Zak, A.; Singh, G. WS2 Nanotube-Embedded SiOC Fibermat Electrodes for Sodium-Ion Batteries. *ACS Omega* **2023**, *8* (11), 10126−10138.
(38) Wang, J.; Yu, L.; Zhou, Z.; Zeng, L.; Wei, M. Template-free synthesis of metallic WS2 hollow microspheres as an anode for the sodium-ion battery. *J. Colloid Interface Sci.* **2019**, *557*, 722−728.
(39) Yang, W.; Wang, J.; Si, C.; Peng, Z.; Zhang, Z. Tungsten diselenide nanoplates as advanced lithium/sodium ion electrode materials with different storage mechanisms. *Nano Res.* **2017**, *10*, 2584−2598.
(40) Choi, S. H.; Kang, Y. C. Sodium ion storage properties of WS 2-decorated three-dimensional reduced graphene oxide microspheres. *Nanoscale* **2015**, *7* (9), 3965−3970.
(41) Barik, G.; Pal, S. Monolayer Transition-Metal Dichalcogenide Mo1−xWxS2 Alloys as Efficient Anode Materials for Lithium-Ion Batteries. *J. Phys. Chem. C* **2018**, *122* (45), 25837−25848.
(42) Tan, T. L.; Ng, M.-F.; Eda, G. Stable Monolayer Transition Metal Dichalcogenide Ordered Alloys with Tunable Electronic Properties. *J. Phys. Chem. C* **2016**, *120* (5), 2501−2508.
(43) Splendiani, A.; Sun, L.; Zhang, Y.; Li, T.; Kim, J.; Chim, C.-Y.; Galli, G.; Wang, F. Emerging Photoluminescence in Monolayer MoS2. *Nano Lett.* **2010**, *10* (4), 1271−1275.
(44) Chen, Y.; Xi, J.; Dumcenco, D. O.; Liu, Z.; Suenaga, K.; Wang, D.; Shuai, Z.; Huang, Y.-S.; Xie, L. Tunable Band Gap Photoluminescence from Atomically Thin Transition-Metal Dichalcogenide Alloys. *ACS Nano* **2013**, *7* (5), 4610−4616.
(45) Suksomboon, M.; Kongsawatvoragul, K.; Duangdangchote, S.; Sawangphruk, M. Reducing the Energy Band Gap of Cobalt Hydroxide Nanosheets with Silver Atoms and Enhancing Their Electrical Conductivity with Silver Nanoparticles. *ACS Omega* **2021**, *6* (32), 20804−20811.
(46) He, Q.; Wan, Y.; Jiang, H.; Wu, C.; Sun, Z.; Chen, S.; Zhou, Y.; Chen, H.; Liu, D.; Haleem, Y. A.; Ge, B.; Wu, X.; Song, L. High-metallic-phase-concentration Mo1−xWxS2 nanosheets with expanded interlayers as efficient electrocatalysts. *Nano Res.* **2018**, *11* (3), 1687−1698.
(47) Tan, Z. H.; Kong, X. Y.; Ng, B.-J.; Soo, H. S.; Mohamed, A. R.; Chai, S.-P. Recent Advances in Defect-Engineered Transition Metal Dichalcogenides for Enhanced Electrocatalytic Hydrogen Evolution: Perfecting Imperfections. *ACS Omega* **2023**, *8* (2), 1851−1863.
(48) Dey, S.; Singh, G. Sodium and potassium ion storage in cation substituted 2D MoWSe2: Insights into the effects of upper voltage cut-off. *Nanotechnology* **2023**, *34*, No. 385401, DOI: 10.1088/1361-6528/acdf66.
(49) Su, D.; Dou, S.; Wang, G. Ultrathin MoS2 Nanosheets as Anode Materials for Sodium-Ion Batteries with Superior Performance. *Adv. Energy Mater.* **2015**, *5* (6), No. 1401205.
(50) Lin, Z.; Thee, M. T.; Elías, A. L.; Feng, S.; Zhou, C.; Fujisawa, K.; Perea-López, N.; Carozo, V.; Terrones, H.; Terrones, M. Facile synthesis of MoS2 and MoxW1-xS2 triangular monolayers. *APL Mater.* **2014**, *2* (9), No. 092514.
(51) Plechinger, G.; Heydrich, S.; Eroms, J.; Weiss, D.; Schüller, C.; Korn, T. Raman spectroscopy of the interlayer shear mode in few-layer MoS2 flakes. *Appl. Phys. Lett.* **2012**, *101* (10), No. 101906.
(52) Qiao, X.-F.; Li, X.-L.; Zhang, X.; Shi, W.; Wu, J.-B.; Chen, T.; Tan, P.-H. Substrate-free layer-number identification of two-dimensional materials: A case of Mo0.5W0.5S2 alloy. *Appl. Phys. Lett.* **2015**, *106* (22), No. 223102.
(53) Song, J.-G.; Ryu, G. H.; Lee, S. J.; Sim, S.; Lee, C. W.; Choi, T.; Jung, H.; Kim, Y.; Lee, Z.; Myoung, J.-M.; Dussarrat, C.; Lansalot-Matras, C.; Park, J.; Choi, H.; Kim, H. Controllable synthesis of molybdenum tungsten disulfide alloy for vertically composition-controlled multilayer. *Nat. Commun.* **2015**, *6* (1), No. 7817.
(54) Dumcenco, D. O.; Chen, K. Y.; Wang, Y. P.; Huang, Y. S.; Tiong, K. K. Raman study of 2H-Mo1−xWxS2 layered mixed crystals. *J. Alloys Compd.* **2010**, *506* (2), 940−943.
(55) David, L.; Bhandavat, R.; Singh, G. MoS2/Graphene Composite Paper for Sodium-Ion Battery Electrodes. *ACS Nano* **2014**, *8* (2), 1759−1770.
(56) Ennaoui, A.; Diesner, K.; Fiechter, S.; Moser, J. H.; Lévy, F. Structural analysis of 2H−WS2 thin films by X-ray and TEM investigation. *Thin Solid Films* **1997**, *311* (1), 146−150.
(57) Wang, H.; Ouyang, L.; Zou, G.; Sun, C.; Hu, J.; Xiao, X.; Gao, L. Optimizing MoS2 Edges by Alloying Isovalent W for Robust Hydrogen Evolution Activity. *ACS Catal.* **2018**, *8* (10), 9529−9536.
(58) Major, G. H.; Fairley, N.; Sherwood, P. M. A.; Linford, M. R.; Terry, J.; Fernandez, V.; Artyushkova, K. Practical guide for curve fitting in x-ray photoelectron spectroscopy. *J. Vac. Sci. Technol., A* **2020**, *38* (6), No. 061203, DOI: 10.1116/6.0000377.
(59) Scanlon, D. O.; Watson, G. W.; Payne, D. J.; Atkinson, G.; Egdell, R. G.; Law, D. S.-L. Theoretical and Experimental Study of the


https://doi.org/10.1021/acsomega.4c01966
*ACS Omega* 2024, 9, 24933−24947

Electronic Structures of MoO3 and MoO2. *J. Phys. Chem. C* **2010**, *114*, 4636−4645.
(60) Liu, Y.; Li, J.; Liu, B.; Chen, Y.; Wu, Y.; Hu, X.; Zhong, G.; Yuan, J.; Chen, J.; Zhan, H.; Wen, Z. Confined WS2 Nanosheets Tubular Nanohybrid as High-Kinetic and Durable Anode for Sodium-Based Dual Ion Batteries. *ChemSusChem* **2023**, *16* (4), No. e202201200.
(61) Peignon, M. C.; Cardinaud, C.; Turban, G. A kinetic study of reactive ion etching of tungsten in SF 6/O 2 RF plasmas. *J. Electrochem. Soc.* **1993**, *140* (2), 505.
(62) Patra, A.; Shaikh, M.; Ghosh, S.; Late, D. J.; Rout, C. S. MoWS 2 nanosheets incorporated nanocarbons for high-energy-density pseudocapacitive negatrode material and hydrogen evolution reaction. *Sustainable Energy Fuels* **2022**, *6* (12), 2941−2954.
(63) Pan, Q.; Zhang, Q.; Zheng, F.; Liu, Y.; Li, Y.; Ou, X.; Xiong, X.; Yang, C.; Liu, M. Construction of MoS2/C Hierarchical Tubular Heterostructures for High-Performance Sodium Ion Batteries. *ACS Nano* **2018**, *12* (12), 12578−12586.
(64) Chong, S.; Sun, L.; Shu, C.; Guo, S.; Liu, Y.; Wang, W.; Liu, H. K. Chemical bonding boosts nano-rose-like MoS2 anchored on reduced graphene oxide for superior potassium-ion storage. *Nano Energy* **2019**, *63*, No. 103868.
(65) Wang, X.; Huang, J.; Li, J.; Cao, L.; Hao, W.; Xu, Z.; Kang, Q. Controlling the layered structure of WS2 nanosheets to promote Na+ insertion with enhanced Na-ion storage performance. *Electrochim. Acta* **2016**, *222*, 1724−1732.
(66) Zhang, R.; Bao, J.; Pan, Y.; Sun, C.-F. Highly reversible potassium-ion intercalation in tungsten disulfide. *Chem. Sci.* **2019**, *10* (9), 2604−2612.
(67) Wang, J.; Luo, C.; Gao, T.; Langrock, A.; Mignerey, A. C.; Wang, C. An Advanced MoS2/Carbon Anode for High-Performance Sodium-Ion Batteries. *Small* **2015**, *11* (4), 473−481.
(68) Li, Y.; Chang, K.; Shangguan, E.; Guo, D.; Zhou, W.; Hou, Y.; Tang, H.; Li, B.; Chang, Z. Powder exfoliated MoS2 nanosheets with highly monolayer-rich structures as high-performance lithium-/sodium-ion-battery electrodes. *Nanoscale* **2019**, *11* (4), 1887−1900.
(69) Wang, P.; Sun, S.; Jiang, Y.; Cai, Q.; Zhang, Y.-H.; Zhou, L.; Fang, S.; Liu, J.; Yu, Y. Hierarchical Microtubes Constructed by MoS2 Nanosheets with Enhanced Sodium Storage Performance. *ACS Nano* **2020**, *14* (11), 15577−15586.
(70) Ghosh, S.; Qi, Z.; Wang, H.; Martha, S. K.; Pol, V. G. WS2 anode in Na and K-ion battery: Effect of upper cut-off potential on electrochemical performance. *Electrochim. Acta* **2021**, *383*, No. 138339.
(71) Soares, D. M.; Singh, G. SiOC functionalization of MoS2 as a means to improve stability as sodium-ion battery anode. *Nanotechnology* **2020**, *31* (14), No. 145403, DOI: 10.1088/1361-6528/ab6480.
(72) Nagy, S. *Kinetics of Radioactive Decay & Growth*, ELTE, KI: Budapest, Hungary; 2010.
(73) Costa, D. G.; Schulte, P. J. Exponential Growth and Decay. In *An Invitation to Mathematical Biology*; Costa, D. G.; Schulte, P. J., Eds.; Springer International Publishing: Cham, 2023; pp 3−10.
(74) Royal Society of Chemistry. The Royal Society of Chemistry's Interactive Periodic Table. https://www.rsc.org/periodic-table/.
(75) Chen, W.; Zhan, X.; Luo, B.; Ou, Z.; Shih, P.-C.; Yao, L.; Pidaparthy, S.; Patra, A.; An, H.; Braun, P. V.; Stephens, R. M.; Yang, H.; Zuo, J.-M.; Chen, Q. Effects of Particle Size on Mg2+ Ion Intercalation into λ-MnO2 Cathode Materials. *Nano Lett.* **2019**, *19* (7), 4712−4720.
(76) Cook, J. B.; Kim, H.-S.; Lin, T. C.; Lai, C.-H.; Dunn, B.; Tolbert, S. H. Pseudocapacitive Charge Storage in Thick Composite MoS2 Nanocrystal-Based Electrodes. *Adv. Energy Mater.* **2017**, 7 (2), No. 1601283.
(77) Wang, J.; Polleux, J.; Lim, J.; Dunn, B. Pseudocapacitive Contributions to Electrochemical Energy Storage in TiO2 (Anatase) Nanoparticles. *J. Phys. Chem. C* **2007**, *111* (40), 14925−14931.
(78) Dong, Y.; Li, D.; Gao, C.; Liu, Y.; Zhang, J. A self-assembled 3D urchin-like Ti0.8Sn0.2O2−rGO hybrid nanostructure as an anode material for high-rate and long cycle life Li-ion batteries. *J. Mater. Chem. A* **2017**, *5* (17), 8087−8094.
(79) Cai, C.; Tao, Z.; Zhu, Y.; Tan, Y.; Wang, A.; Zhou, H.; Yang, Y. A nano interlayer spacing and rich defect 1T-MoS2 as cathode for superior performance aqueous zinc-ion batteries. *Nanoscale Adv.* **2021**, *3* (13), 3780−3787.
(80) Chen, Y.; Yue, M.; Liu, C.; Zhang, H.; Yu, Y.; Li, X.; Zhang, H. Long Cycle Life Lithium Metal Batteries Enabled with Upright Lithium Anode. *Adv. Funct. Mater.* **2019**, *29* (15), No. 1806752.
(81) Wen, C. J.; Boukamp, B. A.; Huggins, R. A.; Weppner, W. Thermodynamic and Mass Transport Properties of " LiAl. *J. Electrochem. Soc.* **1979**, *126* (12), 2258.
(82) Li, W.; Bashir, T.; Wang, J.; Zhou, S.; Yang, S.; Zhao, J.; Gao, L. Enhanced Sodium-Ion Storage Performance of a 2D MoS2 Anode Material Coated on Carbon Nanotubes. *ChemElectroChem* **2021**, *8* (5), 903−910.
(83) Zhang, X.; Ma, T.; Fang, T.; Gao, Y.; Gao, S.; Wang, W.; Liao, L. A novel MoS2@C framework architecture composites with three-dimensional cross-linked porous carbon supporting MoS2 nanosheets for sodium storage. *J. Alloys Compd.* **2020**, *818*, No. 152821.
(84) Hu, J.; Xie, Y.; Zhou, X.; Zhang, Z. Engineering Hollow Porous Carbon-Sphere-Confined MoS2 with Expanded (002) Planes for Boosting Potassium-Ion Storage. *ACS Appl. Mater. Interfaces* **2020**, *12* (1), 1232−1240.
(85) Du, X.; Huang, J.; Guo, X.; Lin, X.; Huang, J.-Q.; Tan, H.; Zhu, Y.; Zhang, B. Preserved Layered Structure Enables Stable Cyclic Performance of MoS2 upon Potassium Insertion. *Chem. Mater.* **2019**, *31* (21), 8801−8809.
(86) Jiang, G.; Xu, X.; Han, H.; Qu, C.; Repich, H.; Xu, F.; Wang, H. Edge-enriched MoS2 for kinetics-enhanced potassium storage. *Nano Res.* **2020**, *13* (10), 2763−2769.


https://doi.org/10.1021/acsomega.4c01966
*ACS Omega* 2024, 9, 24933−24947